applied system innovation

MDPI

Article

Adaptive Inertia and Damping Tuning for VSG Using Improved Harris Hawks Optimization

Rencai Hao [1], Tinglong Pan [1,*], Tianle Yin [2,*], Zhenyang Cai [1], Dezhi Xu [3] and Chengxi Zhang [1]

[1] School of Automation and Intelligent Science, Jiangnan University, Wuxi 214122, China; 6241915009@stu.jiangnan.edu.cn (R.H.); 6231915007@stu.jiangnan.edu.cn (Z.C.); cxzhang@jiangnan.edu.cn (C.Z.)
[2] School of Aeronautics and Astronautics, Sun Yat-sen University, Shenzhen 518107, China
[3] School of Electrical Engineering, Southeast University, Nanjing 210096, China; xudezhi@seu.edu.cn
* Correspondence: tlpan@jiangnan.edu.cn (T.P.); yintle@mail2.sysu.edu.cn (T.Y.)

Abstract

Conventional virtual synchronous generator (VSG) control with fixed parameters cannot simultaneously achieve fast transient response and effective overshoot suppression, while adaptive VSG performance depends strongly on empirically tuned gains. This paper proposes an adaptive VSG control method based on an improved Harris Hawks optimization (IHHO) algorithm. Bounded nonlinear adaptation laws based on arctangent and hyperbolic tangent functions are developed to achieve smooth adjustment of virtual inertia and damping within prescribed limits. A dimensionless multi-index objective function is constructed by combining a normalized time-weighted active-power tracking index with an overshoot index, thereby balancing tracking accuracy, transient convergence, and overshoot suppression. To improve the optimization process, the Golden Sine strategy is introduced into the exploration stage to enhance search directionality, while Cauchy mutation is employed to maintain population diversity and improve the ability to escape local optima. Under consecutive active-power steps from 0 to 10 kW and from 10 to 20 kW, the proposed IHHO achieves overshoots of 5.7% and 7.2%, with settling times of 0.27 s and 0.24 s, respectively. Compared with the unoptimized adaptive VSG, the overshoot is reduced by 9.4 and 9.7 percentage points, while the settling time is shortened by 0.14 s and 0.13 s, respectively. Furthermore, the frequency-response analysis shows approximately 50% reductions in the magnitudes of the negative frequency-deviation peaks and approximately 41% reductions in the negative ROCOF peaks under the investigated conditions. Comparisons with the Grey Wolf Optimizer and conventional Harris Hawks optimization further demonstrate the effectiveness of the proposed IHHO-based adaptive gain-tuning method.

Keywords: virtual synchronous generator; adaptive parameter control; multi-index optimization; improved Harris Hawks optimization

Check for updates

Academic Editor: Igor Korobiichuk

Received: 23 September 2026
Revised: 27 October 2026
Accepted: 30 October 2026
Published: 31 October 2026

Copyright: © 2026 by the authors. Published by MDPI on behalf of the International Institute of Knowledge Innovation and Invention. Licensee MDPI, Basel, Switzerland. This article is an open access article distributed under the terms and conditions of the Creative Commons Attribution (CC BY) license.

1. Introduction

With the increasing penetration of wind power, photovoltaic generation, and energy storage, modern power systems are becoming increasingly dominated by power electronic converters. The reduction in the proportion of conventional synchronous generation creates challenges for frequency stability and dynamic support. Virtual synchronous generator (VSG) control addresses these challenges by reproducing the inertial and damping characteristics of synchronous generators and has received considerable attention in renewable-energy integration and microgrid applications [1–3]. Studies have examined improved

virtual-inertia algorithms and synchronverter-based implementations [4,5], as well as converter-based virtual inertia and the frequency stability of grid-forming converters [6,7]. Other research has investigated transient power-angle stability and droop-based coordination [8,9]. Frequency regulation has also been studied for grid-forming PMSG-based wind turbines and weak-grid renewable-energy stations [10,11], while VSG-based frequency regulation for grid-connected photovoltaic systems and broader multi-area load-frequency control have also been explored [12,13].

The dynamic characteristics of a VSG are strongly influenced by the virtual inertia J and the equivalent damping coefficient D_p. Previous studies have examined transient angle stability in systems containing synchronous and virtual synchronous generators, as well as energy-storage-based VSG coordination [14,15]. Virtual-inertia control in islanded microgrids and inertial-droop or virtual synchronous machine implementations have also been investigated [16–18]. Increasing J can suppress rapid frequency variations, but excessive inertia may slow the transient response. Increasing D_p improves damping and suppresses power oscillations and overshoot, whereas excessive damping may prolong the settling process. Consequently, fixed parameter settings cannot readily maintain a satisfactory compromise between response speed and transient performance under different operating conditions.

The performance of adaptive VSG control also depends on the gains governing the adaptation laws. In this study, the virtual-inertia adaptation gain k_j and the damping adaptation gain k_d determine the adjustment intensity of the corresponding nonlinear control laws. Improper gain selection may lead either to insufficient transient support or to excessive parameter variation, making empirical or trial-and-error tuning difficult. An appropriate optimization framework is therefore needed to evaluate candidate gain combinations while accounting for active-power tracking, transient duration, and overshoot suppression.

Harris Hawks optimization (HHO) is a population-based metaheuristic that alternates between exploration and exploitation according to the escape behavior of prey [19]. However, the exploration process may lack sufficient search directionality, while the progressive concentration of the population around the current optimum can reduce diversity during later iterations. The Sine Cosine Algorithm is another trigonometric metaheuristic for continuous optimization [20]. The Golden Sine Algorithm combines sinusoidal position updating with golden-section information and can enhance search directionality [21,22]. Cauchy-based mutation has been used in other metaheuristic algorithms to combine local perturbations with occasional large search steps [23]. A previous HHO variant also combined the inverse cumulative function of the Cauchy distribution with a tangent-flight operator [24]. Evolutionary programming has also been studied as a population-based optimization approach [25]. Moreover, the no-free-lunch theorems indicate that no optimization algorithm is uniformly superior across all possible optimization problems. Therefore, the effectiveness of an optimizer should be evaluated for the specific optimization task under consideration [26].

Recent studies have investigated various approaches to adaptive VSG control and parameter optimization. Fuzzy adaptive inertia control under state-of-charge constraints and fuzzy self-adaptive control for hybrid microgrids have been studied [27,28]. Coordinated self-adaptive frequency regulation and communication-free adaptive virtual-inertia control have also been investigated [29,30]. Other studies address adaptive inertia and damping, including adaptive optimal tuning [31,32]. Beyond adaptive control laws, differential evolution (DE) is a population-based method for continuous optimization [33], and its combination with fuzzy logic has been applied to VSG parameter optimization [34]. Deep reinforcement learning-based parameter self-tuning has also been investigated [35].

These studies address different aspects of adaptive control and parameter tuning. Building on this research, the present work focuses on the joint optimization of the virtual-inertia and damping adaptation gains k_j and k_d in the proposed nonlinear adaptive control laws. A dimensionless multi-index objective function is formulated to balance time-weighted active-power tracking performance and transient overshoot. Furthermore, an improved Harris Hawks optimization algorithm (IHHO) is developed by integrating the Gold-SA exploration strategy to improve search directionality and probabilistic Cauchy mutation to enhance population diversity. The methodological contribution lies in coordinating these optimization mechanisms with the adaptive control laws and the multi-index objective function for constrained joint gain tuning, rather than claiming either mechanism as a novel standalone operator. The effectiveness of the proposed framework is evaluated through comparative simulations and ablation experiments.

Contribution

The main contributions of this work are summarized as follows:

(1) A bounded nonlinear adaptive control mechanism is designed for the VSG. Arctangent and hyperbolic tangent functions are combined to establish smooth state-dependent adjustment laws for virtual inertia and damping, allowing the controller to provide stronger transient support during disturbances while gradually recovering toward the nominal operating state and avoiding abrupt or excessive parameter variation.

(2) A multi-index optimization objective is constructed for adaptive-gain tuning.A time-weighted active-power tracking index and a transient overshoot index are formulated in dimensionless form and integrated through a weighted aggregation strategy. This formulation simultaneously accounts for tracking accuracy, transient duration, and overshoot suppression, providing a quantitative alternative to trial-and-error gain selection.

(3) An improved HHO algorithm is developed by integrating the Gold-SA exploration strategy and probabilistic Cauchy mutation. Gold-SA is introduced to improve search directionality, whereas Cauchy mutation enhances population diversity and provides opportunities to escape local optima. By combining these complementary mechanisms, the proposed IHHO aims to improve the search performance in the joint optimization of the virtual-inertia and damping adaptation gains.

2. VSG Active Power–Frequency Model and Parameter Adaptive Control Strategy

2.1. Control Structure of the VSG Grid-Connected Inverter

Figure 1 shows the control structure of the VSG grid-connected inverter. A three-phase voltage-source inverter is used as the main circuit, with the PCC voltages and currents sampled to obtain the system states. After coordinate transformation and power calculation, the active power P and reactive power Q are obtained. Based on P_{ref}, Q_{ref}, and the measured output power, the VSG control loop generates the angular frequency ω, phase angle θ, and internal electromotive force E, while the voltage/current dual-loop controller and SPWM generate the switching signals. Since this study focuses on the VSG dynamic response under active-power disturbances, the following analysis mainly considers the effects of J and D_p in the active power–frequency loop.

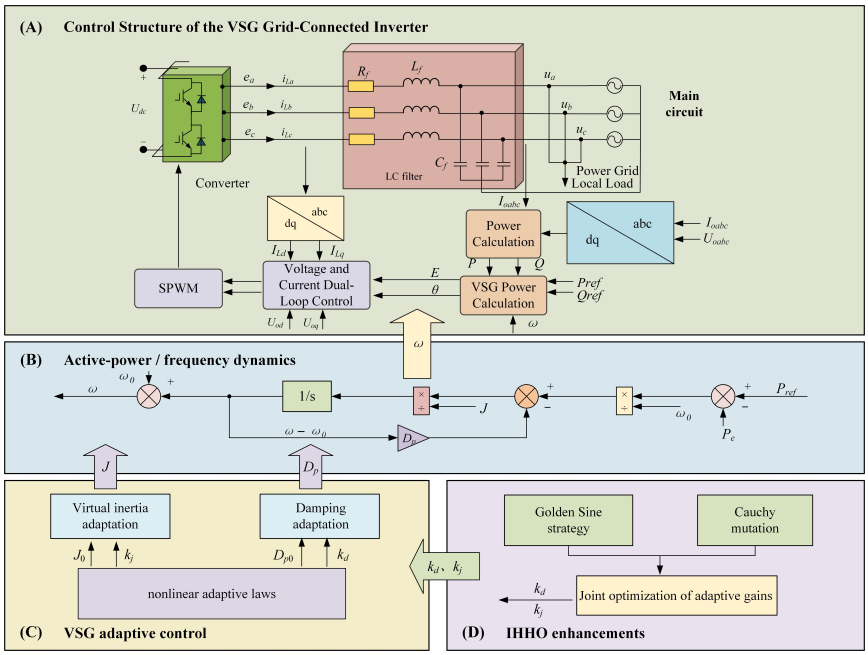


Figure 1. Overall Framework of IHHO-Based Adaptive Parameter Control for VSG.

2.2. Analysis of VSG Active Power–Frequency Dynamic Characteristics

By emulating the rotor motion characteristics of a conventional synchronous generator, the VSG enables the grid-connected inverter to provide a certain degree of virtual inertia and damping support. Its active power–frequency dynamic characteristics can be described by the rotor motion equation of a synchronous generator as follows:

$$\begin{cases} J\dfrac{d\omega}{dt} = T_m - T_e - D(\omega - \omega_0) \\ \dfrac{d\theta}{dt} = \omega - \omega_0 \end{cases} \tag{1}$$

where J is the rotor moment of inertia; T_m is the mechanical torque; T_e is the electromagnetic torque; D is the damping coefficient; and ω and ω_0 denote the actual angular frequency and rated angular frequency of the VSG, respectively.

To emulate the primary frequency regulation characteristics of a synchronous generator, the VSG adopts active power–frequency droop control, and its equivalent mechanical power reference can be expressed as:

$$P_m = P_{\text{ref}} + k_p(\omega_0 - \omega) \tag{2}$$

where P_{ref} is the reference active power, and k_p is the active power–frequency droop coefficient.

By converting the torque terms into power form and combining them with Equation (2), the VSG active power–frequency dynamics are linearized around the rated angular frequency ω_0. Defining the equivalent damping coefficient as $D_p = (k_p + D\omega_0)/\omega_0$, the resulting control structure is illustrated in Region B of Figure 1.

As shown in Region B of Figure 1, J and D_p are the key parameters governing the VSG active power–frequency dynamics. Small-signal analysis around the equilibrium point gives the natural frequency and damping ratio as:

$$\begin{cases} \omega_n = \sqrt{\dfrac{K_s}{J\omega_0}} \\ \zeta = \dfrac{D_p}{2}\sqrt{\dfrac{\omega_0}{JK_s}} \end{cases} \tag{3}$$

where K_s is the synchronizing power coefficient.

The selection of the virtual inertia J and damping coefficient D_p should satisfy both frequency stability requirements and transient dynamic performance constraints. Under steady-state conditions, the active power–frequency characteristic of the VSG follows the droop relationship. To ensure that the steady-state angular frequency deviation does not exceed the allowable limit $\Delta\omega_{\text{allow}}$ under the maximum power deficit $\Delta P_{\max}$, the damping coefficient should satisfy:

$$D_p \geq D_{p\min} = \frac{\Delta P_{\max}}{\omega_0 \Delta\omega_{\text{allow}}} \tag{4}$$

where $\Delta P_{\max}$ is the maximum active power deficit and $\Delta\omega_{\text{allow}}$ is the allowable angular frequency deviation. To achieve a reasonable compromise between oscillation suppression and dynamic response, the damping ratio is selected as $\zeta = 0.707$. According to Equation (3), the corresponding reference damping coefficient can be derived as:

$$D_{p,\text{ref}} = 2\zeta\sqrt{\frac{JK_s}{\omega_0}} \approx 1.414\sqrt{\frac{JK_s}{\omega_0}} \tag{5}$$

The virtual inertia J determines the ability of the VSG to suppress rapid frequency variations. During a sudden power disturbance, the initial rate of change of frequency (RoCoF) is mainly governed by the inertial response. To satisfy the allowable maximum angular frequency variation rate, the lower bound of virtual inertia can be expressed as:

$$J \geq J_{\min} = \frac{\Delta P_{\text{step}}}{\omega_0 \left|\frac{d\omega}{dt}\right|_{\max}} \tag{6}$$

where ΔP_{step} represents the active power disturbance magnitude, and $|d\omega/dt|_{\max}$ denotes the allowable maximum angular frequency variation rate. However, excessive virtual inertia may slow down the system response. For an approximately second-order system, the settling time under the 2% tolerance criterion can be estimated as:

$$\begin{cases} t_s \approx \dfrac{4}{\zeta\omega_n} = \dfrac{4}{\zeta}\sqrt{\dfrac{J\omega_0}{K_s}} \leq t_{\text{req}}, \\ J \leq J_{\max} = \dfrac{(t_{\text{req}}\zeta)^2 K_s}{16\omega_0}. \end{cases} \tag{7}$$

where t_{req} denotes the maximum allowable settling time. Therefore, the selection of J and D_p should consider frequency deviation, RoCoF, damping performance, and settling time simultaneously. These constraints provide a theoretical basis for determining the allowable parameter ranges in the subsequent adaptive control strategy.

Equation (3) shows that increasing J lowers the natural oscillation frequency and smooths frequency variations, but excessive inertia slows the dynamic response. Increasing

D_p improves damping and suppresses power oscillations and overshoot, whereas excessive damping may prolong the settling process. Therefore, fixed J and D_p values cannot easily balance response speed, overshoot suppression, and stability.

It should be noted that the small-signal relations in Equation (3) are derived under the assumption that J and D_p are constant around an equilibrium point. In the proposed adaptive controller, both parameters vary with the system operating state within their prescribed bounds. Therefore, the fixed-parameter small-signal analysis provides a theoretical reference for parameter selection but does not, by itself, establish the stability of the complete time-varying system. The bounded frequency-deviation and ROCOF responses observed in the simulations indicate satisfactory transient behavior under the investigated operating conditions; however, they do not constitute a general stability proof for all possible conditions. A rigorous stability analysis of the complete time-varying adaptive system remains an important direction for future research.

2.3. Adaptive Control Strategy for Virtual Inertia and Damping Parameters

When the active power command changes, the VSG angular frequency and its rate of change exhibit transient variations. A large rate of change requires an increase in J to suppress rapid frequency variation, while a large frequency deviation requires a higher D_p to reduce oscillations and power overshoot. As the transient response subsides, J and D_p approach the steady-state values determined by the adaptive laws and the prescribed saturation bounds. When the frequency deviation approaches zero, the adaptive laws drive J and D_p toward their nominal values J_0 and D_{p0}, respectively, provided that these nominal values satisfy the prescribed bounds.

To achieve smooth and continuous parameter adjustment, nonlinear adaptive laws based on the arctan and tanh functions are adopted. Their smooth and saturating characteristics allow J and D_p to vary with the frequency deviation and its rate of change, while upper and lower bounds prevent parameter violations. The corresponding piecewise adaptive functions are expressed as:

$$J^*(x_1, x_2) = J_0 + \frac{2k_j \arctan(10|x_1|)}{\pi}\left[\frac{1+\tanh(0.1x_1x_2)}{2} + 0.1\frac{1-\tanh(0.1x_1x_2)}{2}\right],$$

$$J(x_1, x_2) = \begin{cases} J_{\max}, & J^*(x_1, x_2) \geq J_{\max}, \\ J_{\min}, & J^*(x_1, x_2) \leq J_{\min}, \\ J^*(x_1, x_2), & J_{\min} < J^*(x_1, x_2) < J_{\max}. \end{cases} \tag{8}$$

$$D_p^*(x_1) = D_{p0} + \frac{3}{2}\pi k_d \tanh(0.1|x_1|),$$

$$D_p(x_1) = \begin{cases} D_{p\max}, & D_p^*(x_1) \geq D_{p\max}, \\ D_{p\min}, & D_p^*(x_1) \leq D_{p\min}, \\ D_p^*(x_1), & D_{p\min} < D_p^*(x_1) < D_{p\max}. \end{cases} \tag{9}$$

where J_0 and D_{p0} are the initial values of the virtual inertia and damping coefficient, respectively; k_j is the adaptive gain of the virtual inertia, which regulates the variation magnitude of J during the transient process; k_d is the adaptive damping gain, which adjusts the variation magnitude of D_p; and $J_{\min}$, $J_{\max}$, $D_{p\min}$, and $D_{p\max}$ denote the lower and upper bounds of the virtual inertia and damping coefficient, respectively. $x_1 = \omega - \omega_0$ denotes the angular frequency deviation (rad/s), and $x_2 = d\omega/dt$ represents the rate of change of angular frequency (rad/s^2), ω and ω_0 are the actual and nominal angular frequencies, respectively.

The proposed adaptive mechanism enables J and D_p to vary continuously with the transient operating state. However, its dynamic performance remains sensitive to the selection of k_j and k_d. Small values may result in insufficient parameter adjustment, whereas excessively large values may lead to over-adjustment and degraded transient performance. Therefore, empirical tuning cannot reliably provide a satisfactory compromise between response speed and overshoot suppression. To address this problem, the next section first formulates a multi-index optimization objective for evaluating active-power tracking and transient overshoot. An improved Harris Hawks optimization method is then developed to solve the resulting optimization problem and determine k_j and k_d systematically.

3. Multi-Index Adaptive-Gain Optimization Based on Improved Harris Hawks Optimization

3.1. Construction of the Multi-Index Optimization Objective

The tuning of k_j and k_d is formulated as a constrained optimization problem. For the i-th candidate solution, the decision vector is defined as

$$\mathbf{X}_i = \left[k_{j,i},\, k_{d,i}\right], \tag{10}$$

subject to

$$0.01 \le k_j \le 3, \qquad 5 \le k_d \le 50. \tag{11}$$

For each candidate solution $\mathbf{X}_i$, the corresponding values of k_j and k_d are transferred to the VSG simulation model. The operating conditions, including the active-power reference profile and disturbance sequence, are predefined in the simulation model. After each simulation, the active-power reference $P_{\mathrm{ref}}(t)$ and the measured active power $P(t)$ are used to evaluate the performance of the candidate solution.

Since the objective of adaptive-gain optimization is to improve active-power tracking while suppressing excessive transient overshoot, the power-tracking error and overshoot are selected as the performance indices.

The normalized active-power tracking error is defined as

$$e_P(t) = \frac{P_{\mathrm{ref}}(t) - P(t)}{P_N}, \tag{12}$$

where P_N denotes the rated active power of the VSG. To penalize both large tracking errors and errors persisting for a long duration, the integral of time-weighted squared error (ITSE) is adopted as the power-tracking performance index:

$$J_P = \frac{2}{T_f^2}\int_0^{T_f} t[e_P(t)]^2 \mathrm{d}t, \tag{13}$$

where T_f denotes the total simulation time. The factor $2/T_f^2$ is introduced to obtain a dimensionless performance index. The time weighting in J_P increases the penalty assigned to tracking errors that persist for a longer duration. Consequently, the index reflects not only the magnitude of the active-power tracking error but also the speed at which the transient response converges. This avoids introducing settling time as a separate discontinuous objective while still accounting for transient duration in the optimization process.

To quantify the transient overshoot, the reference-power transitions contained in $P_{\mathrm{ref}}(t)$ are identified from the simulation model. For the m-th reference transition, the power variation is expressed as

$$\Delta P_m = P^{+}_{\mathrm{ref},m} - P^{-}_{\mathrm{ref},m}, \tag{14}$$

where $P^{-}_{\mathrm{ref},m}$ and $P^{+}_{\mathrm{ref},m}$ denote the active-power references immediately before and after the m-th transition, respectively. The direction of the reference variation is defined as

$$s_m = \mathrm{sgn}(\Delta P_m). \tag{15}$$

Accordingly, the overshoot ratio associated with the m-th reference transition is defined as

$$M_{p,m} = \max_{t \in \Omega_m} \left\{ \max \left[0, \frac{s_m \left(P(t) - P^{+}_{\mathrm{ref},m} \right)}{|\Delta P_m|} \right] \right\}, \tag{16}$$

where Ω_m denotes the transient observation interval corresponding to the m-th reference transition. This definition is applicable to both increasing and decreasing active-power commands. When N_s reference-power transitions occur during the simulation, the overall overshoot performance index is defined as

$$J_O = \frac{1}{N_s} \sum_{m=1}^{N_s} M_{p,m}. \tag{17}$$

Both J_P and J_O are dimensionless. Therefore, the overall fitness function for adaptive-gain optimization is formulated as

$$F(k_j, k_d) = \lambda_P J_P + \lambda_O J_O, \tag{18}$$

where λ_P and λ_O denote the weighting coefficients associated with active-power tracking performance and overshoot suppression, respectively, satisfying

$$\lambda_P + \lambda_O = 1, \qquad \lambda_P \geq 0, \qquad \lambda_O \geq 0. \tag{19}$$

The two indices characterize different aspects of the transient response. The tracking index reflects both tracking accuracy and convergence behavior, whereas the overshoot index explicitly penalizes excessive transient peaks. Since both indices are dimensionless, their relative importance can be adjusted directly through the weighting coefficients. The weighted formulation therefore provides an explicit trade-off between active-power tracking performance and overshoot suppression without allowing either index to dominate merely because of its numerical scale.The weighting coefficients determine the relative importance assigned to active-power tracking and overshoot suppression. Once selected, the same weighting coefficients are used for all optimization algorithms to ensure a consistent and fair comparison.In this study, the weighting coefficients are set to $\lambda_P = 0.5$ and $\lambda_O = 0.5$, assigning equal weights to active-power tracking performance and overshoot suppression in the objective function.

A smaller value of $F(k_j, k_d)$ indicates better overall transient performance. Candidate solutions that result in simulation failure, numerical divergence, or unstable operation are assigned a sufficiently large penalty fitness value so that they are excluded from the subsequent optimal-solution selection.

3.2. Basic Principles and Limitations of HHO

The HHO algorithm is a swarm intelligence method. Its search process includes global exploration and local exploitation, with the current best individual regarded as the prey. The transition between the two stages is governed by the prey escape energy E:

$$E(t) = 2E_0\left(1 - \frac{t}{T}\right) \tag{20}$$

where $E_0 \in [-1, 1]$ is the randomly generated initial escape energy of the prey, t denotes the current iteration number, and T is the maximum number of iterations.

When $|E| \geq 1$, HHO performs global exploration; when $|E| < 1$, it switches to local exploitation using strategies such as soft besiege, hard besiege, and Lévy-flight-based rapid dives. Although HHO has a simple structure and few control parameters, its exploration stage is highly random and lacks search directionality. Moreover, population diversity decreases as iterations proceed, increasing the risk of local optima. Therefore, HHO is improved by enhancing global exploration directionality and strengthening its ability to escape local optima.

3.3. Exploration Mechanism Based on the Golden Sine Strategy

To reduce the randomness and improve the search directionality of HHO, the Gold-SA is introduced into the exploration stage. By combining sinusoidal search with the golden-section mechanism, Gold-SA improves the use of current optimal information while maintaining population diversity.

Specifically, Gold-SA modifies the hawk position update rule. With the golden ratio $\tau \approx 0.618$, when $|E| \geq 1$ at the t-th iteration, the position update equation is given by:

$$X_{\text{new}}(t+1) = X_i(t)|\sin(R_1)| - R_2 \sin(R_1)\left|g_1 X_{\text{prey}}(t) - g_2 X_i(t)\right|. \tag{21}$$

where $X_i(t)$ is the position of the i-th hawk at iteration t, and $X_{\text{prey}}(t)$ is the current global optimum. $R_1 \in [0, 2\pi]$ and $R_2 \in [0, \pi]$ are random variables. The golden-section coefficients are defined as $g_1 = -\pi + (1 - \tau) \cdot 2\pi$ and $g_2 = -\pi + \tau \cdot 2\pi$, respectively, to regulate the search range.

This update strengthens the guidance of the current optimum, reduces blind random exploration, and provides better candidate regions for subsequent local exploitation.

3.4. Cauchy Mutation Strategy and IHHO Algorithm Procedure

During later iterations, the HHO population converges toward the current optimum, reducing population diversity and increasing the risk of premature convergence. To improve the ability to escape local optima, a Cauchy Mutation Mechanism (CMM) is introduced after position updating. Due to its heavy-tailed distribution, Cauchy mutation can generate both local perturbations and occasional large search steps, thereby preserving local exploitation while enhancing global exploration.

Wang et al. proposed an HHO variant that combines the inverse cumulative function of the Cauchy distribution with a tangent-flight operator [24]. In contrast, the proposed IHHO integrates Gold-SA-based exploration into the exploration stage and applies probabilistic Cauchy mutation to the current global optimum after position updating. The mutated candidate is accepted only if it yields a lower objective-function value. Therefore, the contribution of this study does not lie in the standalone use of Cauchy-based operators, but in the coordination of Gold-SA-based exploration and probabilistic Cauchy mutation within the HHO framework, and their application to the constrained joint optimization of the VSG adaptation gains k_j and k_d using the proposed multi-index objective function.

Accordingly, the current global optimum X_{prey} is subjected to the following Cauchy mutation operation:

$$X^*_{\text{prey}} = X_{\text{prey}} + \alpha \cdot C \tag{22}$$

where C is a perturbation vector independently sampled from the standard Cauchy distribution in each dimension, and α is the scaling factor used to regulate the mutation intensity. A commonly used and numerically stable sampling method is the inverse transform method:

$$C = \gamma \cdot \tan(\pi(u - 0.5)), \qquad u \sim U(0,1) \tag{23}$$

where γ is the scale parameter ($\gamma > 0$), which controls the width of the distribution.

The Cauchy perturbation vector **C** is substituted into Eq. (22) to generate a mutated candidate X^*_{prey}. The fitness of the mutated candidate is evaluated using the objective function defined in Section 3.1. If the mutated candidate provides a lower fitness value than the current global optimum, it replaces X_{prey}; otherwise,the original global optimum is retained. To avoid excessive perturbation of the exploitation process, Cauchy mutation is applied to the current optimal solution with probability P_c. In this study, the Cauchy mutation scaling factor is set to $\alpha = 0.1$, the scale parameter of the Cauchy distribution is set to $\gamma = 1$, and the mutation probability is set to $P_c = 0.2$. These parameters are kept fixed throughout the optimization process.

The heavy-tailed property of the Cauchy distribution enables the current optimum to perform local neighborhood search while retaining the possibility of large-step perturbations, thereby improving the ability to escape local optima. Combined with the Gold-SA exploration strategy, the proposed method improves both the global search directionality and the population diversity of conventional HHO, forming the IHHO algorithm.

In summary, the Gold-SA strategy is employed to enhance the search directionality of HHO during the exploration stage, while Cauchy mutation is introduced to improve the algorithm's ability to escape from local optima during the later stages of iteration, thereby forming the IHHO algorithm. The overall optimization procedure of the proposed IHHO is illustrated in Figure 2.

During each IHHO iteration, the fitness value of each candidate solution is calculated according to Equation (18), and the candidate with the minimum fitness is regarded as the current global optimum X_{prey}. The HHO framework described in Section 3.2 is used as the basic search mechanism, the Gold-SA-based exploration strategy presented in Section 3.3 enhances global exploration, and the Cauchy mutation mechanism introduced in Section 3.4 is employed to improve the ability to escape from local optima. The optimization process continues until the maximum number of iterations is reached. The optimal adaptive gains are finally obtained as

$$\left[k_j^*, k_d^*\right] = \underset{0.01 \le k_j \le 3, 5 \le k_d \le 50}{\arg\min} F(k_j, k_d). \tag{24}$$

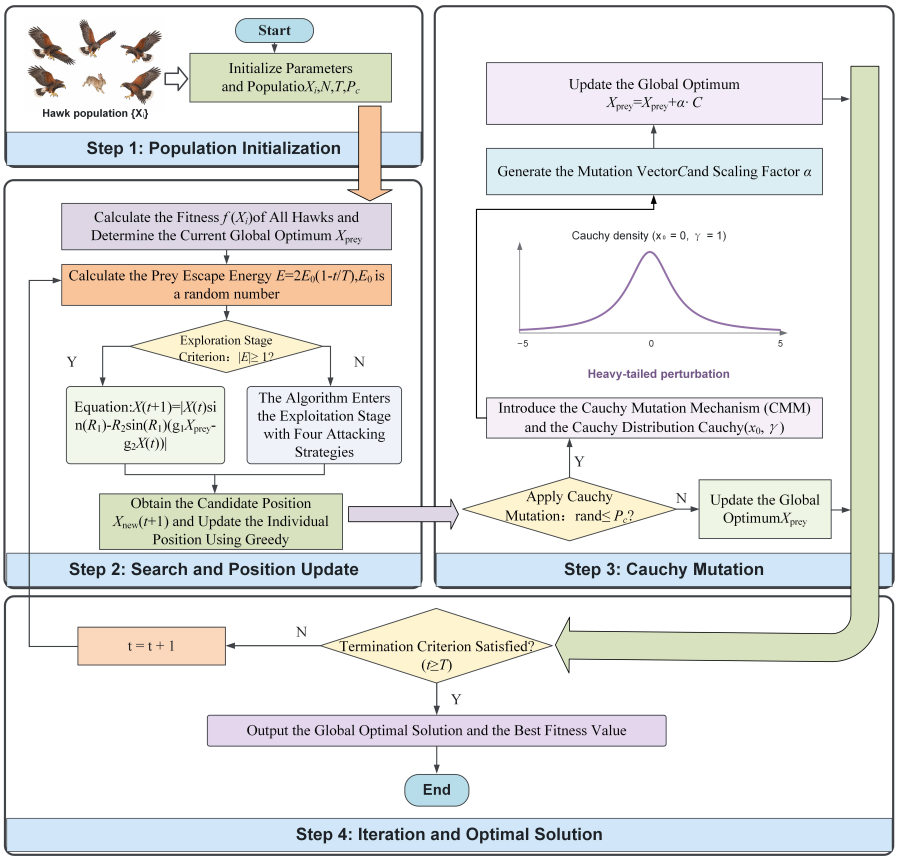


Figure 2. Flowchart of the IHHO Algorithm Integrating the Golden Sine Strategy and Cauchy Mutation.

4. Simulation Validation and Performance Analysis

4.1. Simulation Parameter Settings

To verify the effectiveness of the proposed IHHO-based VSG adaptive parameter control strategy, a grid-connected inverter simulation model is established in MATLAB/Simulink. The system and control parameters are listed in Table 1, while the optimization and performance-evaluation settings are summarized in Table 2.

To ensure that the virtual inertia and damping parameters remain within reasonable ranges throughout the adaptive adjustment process, the parameter variation ranges are set as $0.01 \leq J \leq 3.5$ and $9.51 \leq D_p \leq 40$, taking into account the system stability requirements and simulation parameter settings.

Table 1. System and Control Parameters.

Parameter	Value	Parameter	Value
DC Voltage/V	800	Rated Output Frequency/Hz	50
Equivalent Inductance L_{eq}/mH	5.2	Switching Frequency/kHz	10
Filter Capacitance/μF	20	Phase Voltage Amplitude/V	311
Rated Power/kW	20	J_0	0.2
D_{p0}	10	Droop Coefficient k_p	3.142
Synchronizing Coefficient K_s	86.6		

All optimization algorithms are evaluated under the same system and operating conditions. The common optimization settings are listed in Table 2. The controller-specific adaptive gains obtained by different optimization methods are presented in Section 4.3.

Table 2. Optimization and Performance-Evaluation Settings.

Parameter	Value	Parameter	Value
Population Size N	30	Maximum Iterations T	50
Search Range of k_j	$[0.01, 3]$	Search Range of k_d	$[5, 50]$
Objective Weight λ_P	0.5	Objective Weight λ_O	0.5
Cauchy Mutation Scale Factor α	0.1	Cauchy Distribution Parameter γ	1
Cauchy Mutation Probability P_c	0.2	Boundary Handling	Boundary Clipping
Observation Window Ω_1	$[0.2, 1.0)$	Observation Window Ω_2	$[1.0, T_f]$
Objective-Evaluation Simulation Duration T_f/s	2	Settling-Time Tolerance	2%

4.2. Dynamic Performance Comparison Between the Fixed-Parameter VSG and the Unoptimized Adaptive VSG

To evaluate the effectiveness of the adaptive parameter control mechanism independently of intelligent optimization, the dynamic responses of the fixed-parameter VSG and the unoptimized adaptive VSG are compared under identical system parameters and operating conditions. In the fixed-parameter VSG, the virtual inertia J and damping coefficient D_p remain constant throughout operation. In contrast, the adaptive VSG adjusts J and D_p in real time according to the angular frequency deviation and its rate of change. The adaptive gains of the unoptimized VSG are set to $k_j = 1.47$ and $k_d = 10$, without applying any intelligent optimization algorithm. This comparison is designed to isolate the contribution of the adaptive control mechanism to the transient response. Two consecutive active-power reference steps are applied at $t_1 = 0.2\,\text{s}$ and $t_2 = 1.0\,\text{s}$, corresponding to power transitions from 0 to 10 kW and from 10 to 20 kW, respectively. The resulting active-power responses are compared in Figure 3, and the corresponding overshoot and settling-time indices are summarized in Table 3.

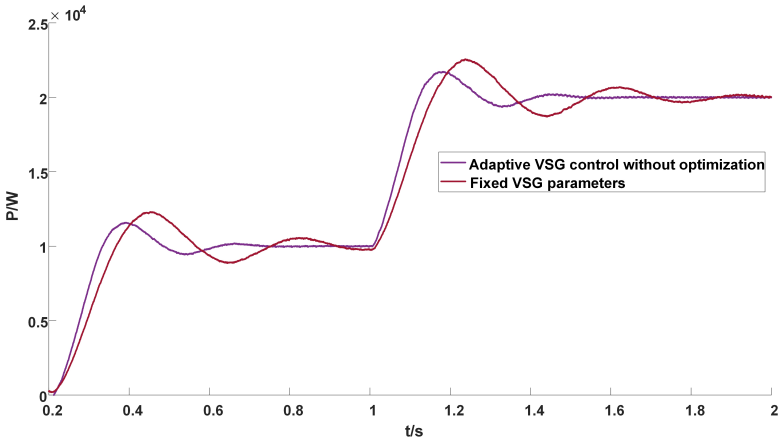


Figure 3. Comparison of Active Power Dynamic Responses Between the Fixed-Parameter VSG and the Unoptimized Adaptive VSG.

Table 3. Dynamic Performance Comparison Between the Fixed-Parameter VSG and the Unoptimized Adaptive VSG.

Step Condition	Control Strategy	Overshoot (%)	Settling Time (s)
$0 \rightarrow 10$ kW	Unoptimized Adaptive VSG	15.1	0.41
	Fixed-Parameter VSG	23.58	0.80
$10 \rightarrow 20$ kW	Unoptimized Adaptive VSG	16.9	0.37
	Fixed-Parameter VSG	26.22	0.67

As shown in Table 3, when the active-power reference steps from 0 to 10 kW at $t = 0.2$ s, the fixed-parameter VSG exhibits an overshoot of 23.58% and a settling time of approximately 0.80 s. With unoptimized adaptive control, the overshoot decreases to 15.1% and the settling time to 0.41 s, corresponding to reductions of 8.48 percentage points and 0.39 s, respectively. At $t = 1.0$ s, the active-power reference increases from 10 to 20 kW. The fixed-parameter VSG exhibits an overshoot of 26.22% and a settling time of approximately 0.67 s. In comparison, the unoptimized adaptive VSG reduces the overshoot to 16.9% and the settling time to 0.37 s, corresponding to reductions of 9.32 percentage points and 0.30 s, respectively. These results demonstrate that adaptive adjustment of the virtual inertia and damping coefficient improves the transient response under consecutive active-power steps. Further improvements through intelligent optimization of the adaptive gains are investigated in Section 4.3.

4.3. Comparison of VSG Dynamic Performance Under Different Optimization Algorithms

4.3.1. Dynamic Performance Comparison

To further evaluate the effectiveness of the proposed IHHO algorithm in optimizing the adaptive gains of the VSG, the dynamic performances of the unoptimized adaptive VSG and the GWO-, HHO-, and IHHO-optimized adaptive VSGs are compared under identical system parameters and operating conditions. The Grey Wolf Optimizer (GWO) is included as a benchmark metaheuristic for comparison [36]. The adaptive gains obtained using the different control strategies are listed in Table 4. The active-power responses under two consecutive reference steps are shown in Figure 4, and the corresponding overshoot and settling-time indices are summarized in Table 5.

Table 4. Adaptive Gains Used by Different Control Strategies.

Control Strategy	J_0	$Dp0$	k_j	k_d
Unoptimized Adaptive VSG	0.2	10	1.47	10
GWO-Optimized Adaptive VSG	0.2	10	1.48	17
HHO-Optimized Adaptive VSG	0.2	10	1.35	20
IHHO-Optimized Adaptive VSG	0.2	10	0.96	30

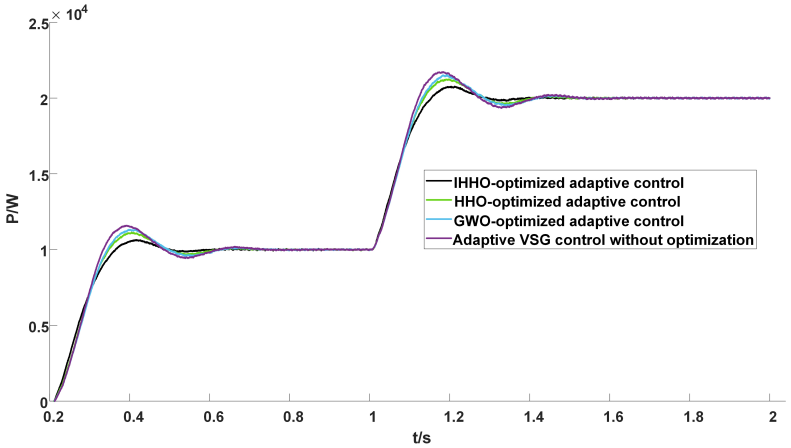


Figure 4. Comparison of Active-Power Dynamic Responses of Adaptive VSGs Under Different Optimization Algorithms.

Table 5. Dynamic Performance Comparison of Adaptive VSGs Under Different Optimization Algorithms.

Step Condition	Control Strategy	Overshoot (%)	Settling Time (s)
0 → 10 kW	Unoptimized Adaptive VSG	15.1	0.41
	GWO-Optimized Adaptive VSG	12.4	0.42
	HHO-Optimized Adaptive VSG	10.5	0.39
	IHHO-Optimized Adaptive VSG	5.7	0.27
10 → 20 kW	Unoptimized Adaptive VSG	16.9	0.37
	GWO-Optimized Adaptive VSG	14.5	0.36
	HHO-Optimized Adaptive VSG	11.9	0.26
	IHHO-Optimized Adaptive VSG	7.2	0.24

As shown in Table 5, for the first active-power reference step from 0 to 10 kW, the unoptimized adaptive VSG exhibits an overshoot of 15.1% and a settling time of 0.41 s. After optimization using GWO, the overshoot decreases to 12.4%, while the settling time is 0.42 s. Although GWO reduces the overshoot by 2.7 percentage points, the settling time increases slightly by 0.01 s. HHO further reduces the overshoot to 10.5% and the settling time to 0.39 s. The proposed IHHO achieves the best performance, with an overshoot of 5.7% and a settling time of 0.27 s, corresponding to reductions of 9.4 percentage points and 0.14 s, respectively, compared with the unoptimized adaptive VSG. For the second active-power reference step from 10 to 20 kW, the unoptimized adaptive VSG exhibits an overshoot of 16.9% and a settling time of 0.37 s. GWO reduces these values to 14.5% and 0.36 s, respectively, whereas HHO achieves an overshoot of 11.9% and a settling time of 0.26 s. The proposed IHHO further reduces the overshoot to 7.2% and the settling time to 0.24 s. Compared with the unoptimized adaptive VSG, these results correspond to reductions of 9.7 percentage points in overshoot and 0.13 s in settling time. Overall, the results show that optimization of the adaptive gains improves the transient performance of the VSG, with IHHO achieving the lowest overshoot and the shortest settling time under both power-step conditions. Compared with GWO and HHO, IHHO provides a more favorable balance between overshoot suppression and response speed.

4.3.2. Frequency Deviation and ROCOF Analysis

To further evaluate the frequency-response characteristics of the four control strategies, the frequency deviation and rate of change of frequency (ROCOF) are analyzed under the two consecutive active-power reference steps at $t = 0.2\,\mathrm{s}$ and $t = 1.0\,\mathrm{s}$. The baseline parameters are kept identical, while the adaptive gains are selected according to the values reported in Section 4.3.1.

As shown in Figure 5, the IHHO-optimized adaptive VSG exhibits smaller frequency excursions, particularly during the negative-deviation stage following each power step. The estimated negative frequency-deviation peaks are approximately $-0.019\,\mathrm{Hz}$ and $-0.021\,\mathrm{Hz}$ for the first and second steps, respectively, compared with approximately $-0.038\,\mathrm{Hz}$ and $-0.042\,\mathrm{Hz}$ for the unoptimized adaptive VSG. These results correspond to reductions of approximately 50% in the magnitudes of the negative frequency deviations. The positive frequency-deviation peaks are also slightly lower than those of the unoptimized strategy. Overall, the results indicate that the IHHO-optimized gains improve frequency- deviation suppression under consecutive power-reference changes.

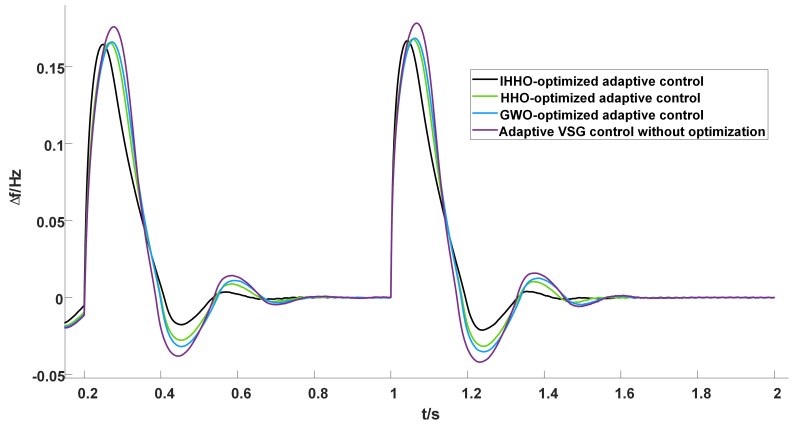


Figure 5. Frequency Deviation Responses of the Four Control Strategies Under Two Consecutive Active−Power Steps.

As shown in Figure 6, the IHHO-based adaptive controller reduces the magnitude of the negative ROCOF peaks and suppresses subsequent oscillations. The estimated negative ROCOF peaks are approximately 1.20 Hz/s and 1.26 Hz/s in magnitude for the two power steps, representing reductions of approximately 41% compared with the corresponding values of the unoptimized adaptive VSG. Moreover, the secondary positive ROCOF peaks decrease from approximately 0.62 Hz/s to 0.26 Hz/s after the first step, and from approximately 0.68 Hz/s to 0.28 Hz/s after the second step. These reductions demonstrate the improved suppression of subsequent ROCOF oscillations. The later negative excursions are also smaller, and the ROCOF curves return close to zero as the transient response subsides.

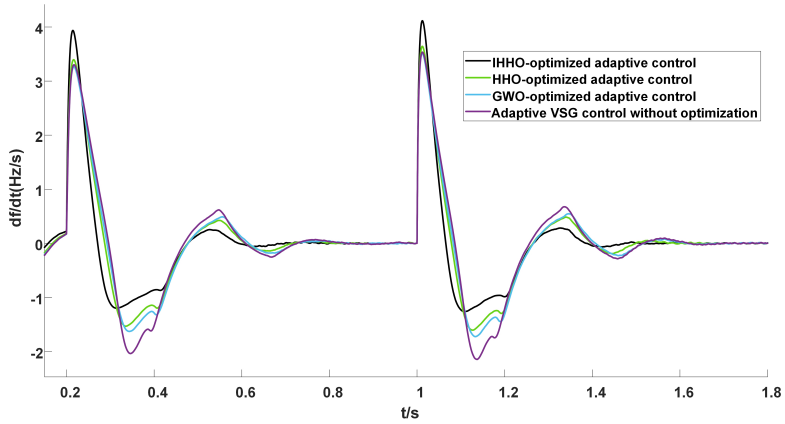


Figure 6. ROCOF Responses of the Four Control Strategies Under Two Consecutive Active−Power Steps.

Taken together, the frequency-deviation and ROCOF responses demonstrate that the IHHO-optimized adaptive control strategy effectively suppresses frequency excursions, reduces negative ROCOF peaks, and mitigates subsequent transient oscillations under consecutive active-power steps. These results complement the active-power response comparisons and further illustrate the benefits of optimizing the adaptive gains.

4.3.3. Adaptive Inertia and Damping Dynamics Under Different Control Strategies

To further investigate the effects of different optimized adaptive gains on the internal dynamics of the VSG controller, the variations in virtual inertia J and damping coefficient D_p are compared under the four control strategies considered in Section 4.3.1. The baseline parameters are kept identical, while the adaptive gains are selected according to the values

reported in the corresponding parameter table. The comparison focuses on the transient adjustment characteristics, subsequent oscillations, and recovery of the adaptive parameters following the two consecutive active-power reference steps.

As shown in Figure 7, the IHHO-optimized adaptive controller exhibits a more moderate virtual-inertia peak than the other three strategies. The peak value is approximately 1.0, whereas the corresponding peaks of the HHO-, GWO-, and unoptimized adaptive controllers are approximately 1.31, 1.41, and 1.42, respectively, as estimated from the plotted curves. In addition, the IHHO curve exhibits relatively small secondary fluctuations following both power steps. The virtual inertia subsequently returns toward its baseline value of $J_0 = 0.2$. These observations indicate that the IHHO-optimized gains produce a more moderate inertia-adjustment trajectory with reduced subsequent oscillations during the transient process.

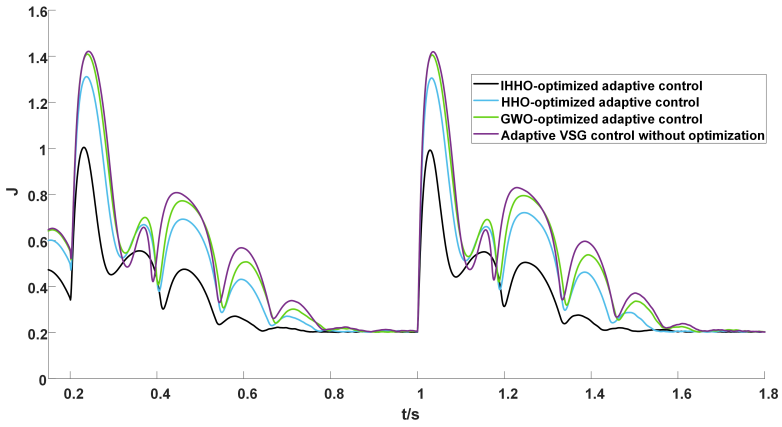


Figure 7. Dynamic Responses of Virtual Inertia J Under Different Control Strategies.

Figure 8 shows that the IHHO-optimized controller produces a more pronounced transient increase in the damping coefficient. Its peak is approximately 21.8, compared with approximately 18.0, 16.9, and 14.3 for the HHO-, GWO-, and unoptimized adaptive controllers, respectively, as estimated from the plotted curves. Following the initial peak, the IHHO-based damping coefficient decreases toward its baseline value of $D_{p0} = 10$, while the subsequent fluctuations remain relatively small. A similar response pattern is observed after the second power step. This behavior illustrates the stronger transient damping adjustment produced by the IHHO-optimized gains and the subsequent recovery of the damping coefficient.

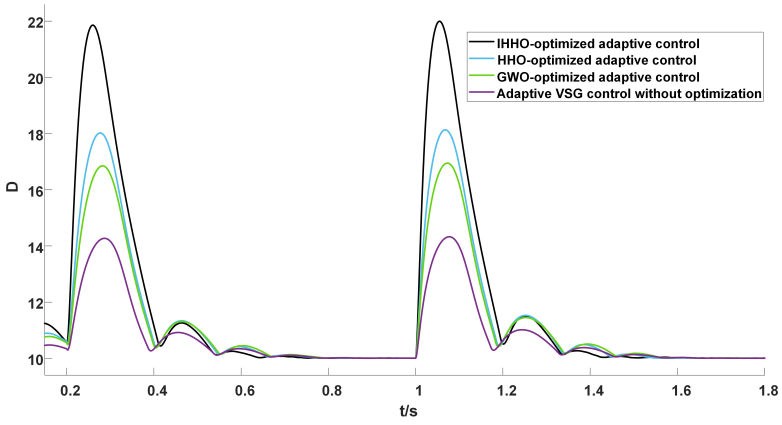


Figure 8. Dynamic Responses of the Damping Coefficient D_p Under Different Control Strategies.

Taken together, the trajectories of J and D_p demonstrate that the optimized adaptive gains influence the two parameters in different but complementary ways. The IHHO-based controller exhibits a more moderate inertia peak and a more pronounced transient damping adjustment, while both parameters return toward their respective baseline values after the power disturbances. These parameter trajectories provide further insight into the adaptive behavior of the proposed controller and complement the active-power and frequency-response comparisons presented in Sections 4.3.1 and 4.3.2.

4.4. Additional Operating Conditions and Disturbance Robustness Analysis

To further evaluate the applicability and disturbance response of the proposed IHHO-based adaptive VSG control strategy, additional simulations and discussions are conducted under operating conditions beyond the baseline comparisons. The analysis considers different active-power reference steps and grid-frequency fluctuations.

4.4.1. Validation Under Different Power-Step Conditions

To further evaluate the adaptability of the proposed IHHO-optimized adaptive VSG control strategy under different power-reference variations, an additional simulation is conducted with three consecutive active-power reference steps. Specifically, the power reference changes from 0 to 5 kW at $t = 0.5$ s, from 5 to 15 kW at $t = 1.5$ s, and from 15 to 10 kW at $t = 2.5$ s. The controller parameters remain unchanged from those used in the preceding sections. The fixed-parameter VSG and the IHHO-optimized adaptive VSG are compared to investigate their transient responses under different step amplitudes and directions. The corresponding peak deviations and settling times are summarized in Table 6.

Table 6. Transient Performance Under Different Power-Step Conditions.

Step Condition	Control Strategy	Peak Deviation (%)	Settling Time (s)
0 → 5 kW	Fixed-Parameter VSG	36	0.77
	IHHO-Optimized Adaptive VSG	12	0.33
5 → 15 kW	Fixed-Parameter VSG	25	0.68
	IHHO-Optimized Adaptive VSG	7	0.26
15 → 10 kW	Fixed-Parameter VSG	38	0.74
	IHHO-Optimized Adaptive VSG	12	0.23

As shown in Figure 9, the IHHO-optimized adaptive VSG exhibits smaller transient power deviations and weaker oscillations than the fixed-parameter VSG under all three power-reference steps. For the first step from 0 to 5 kW, the peak power of the IHHO-based controller is approximately 5.6 kW, whereas that of the fixed-parameter VSG reaches approximately 6.8 kW. The corresponding overshoot magnitudes are approximately 0.6 kW and 1.8 kW, respectively, equivalent to overshoot rates of approximately 12% and 36% relative to the step amplitude. The estimated settling times, based on the 2% error band, are approximately 0.33 s for the IHHO-based controller and 0.77 s for the fixed-parameter VSG. These results indicate that the proposed controller reduces the initial overshoot and accelerates the recovery of the active power.

For the second step from 5 to 15 kW, the peak power of the fixed-parameter VSG reaches approximately 17.5 kW, while that of the IHHO-based controller is approximately 15.7 kW. The corresponding overshoot magnitudes are approximately 2.5 kW and 0.7 kW, representing overshoot rates of approximately 25% and 7%, respectively, relative to the 10 kW step amplitude. The estimated settling times are approximately 0.68 s for the fixed-

parameter VSG and 0.26 s for the IHHO-based controller. In addition to the smaller overshoot, the IHHO-based controller exhibits a smoother recovery process, whereas the fixed-parameter VSG shows a pronounced undershoot and subsequent oscillations before approaching the new reference value.

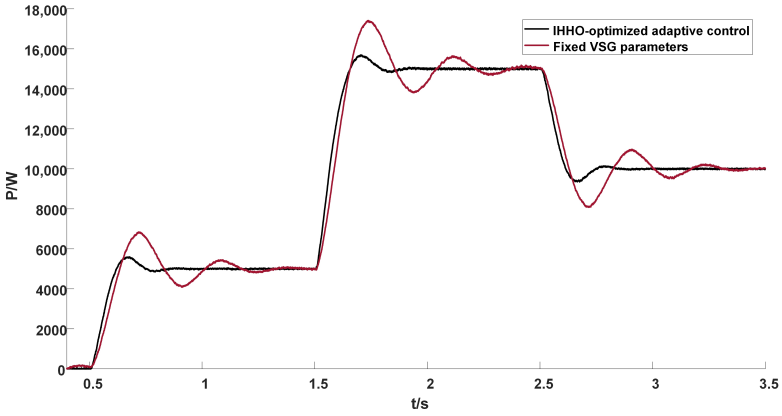


Figure 9. Active−Power Responses of the Fixed−Parameter VSG and the IHHO−Optimized Adaptive VSG Under Three Consecutive Power−Reference Steps.

The third step, from 15 to 10 kW, examines the response to a decreasing power reference. The minimum output power of the fixed-parameter VSG is approximately 8.1 kW, compared with approximately 9.4 kW for the IHHO-based controller. The corresponding undershoot magnitudes are approximately 1.9 kW and 0.6 kW, equivalent to approximately 38% and 12% of the 5 kW step amplitude, respectively. The estimated settling times are approximately 0.74 s for the fixed-parameter VSG and 0.23 s for the IHHO-based controller. The smaller undershoot and weaker subsequent oscillations demonstrate the improved response to a downward power-reference change.

Overall, the additional simulation demonstrates that the IHHO-optimized adaptive VSG provides improved transient active-power regulation under both increasing and decreasing power-reference steps. Compared with the fixed-parameter VSG, the proposed controller reduces the overshoot or undershoot and shortens the settling time in all three tested cases. Importantly, the same optimized adaptive gains are retained throughout the entire simulation without re-optimization for individual operating conditions. These results provide further evidence of the adaptability of the proposed control strategy under different power-reference variations.

4.4.2. Robustness Under Grid-Frequency Fluctuations

To further evaluate the robustness of the proposed IHHO-optimized adaptive VSG control strategy against grid-frequency disturbances, an additional simulation is conducted with a constant active-power reference of 20 kW. At $t = 3.0$ s, the grid frequency increases from 50 to 50.2 Hz and remains at this level for 0.1 s. At $t = 3.1$ s, the grid frequency returns to its nominal value of 50 Hz. The fixed-parameter VSG and the IHHO-optimized adaptive VSG are compared using the same controller parameters as those in the preceding simulations. The frequency deviation in this test is calculated as the difference between the instantaneous VSG frequency and the grid frequency.

As shown in Figure 10, the grid-frequency disturbance causes a noticeable active-power reduction in both control strategies. The minimum power of the fixed-parameter VSG is approximately 11.1 kW, whereas that of the IHHO-optimized adaptive VSG is approximately 12.3 kW. Relative to the initial power of 20 kW, the maximum power reduction decreases from approximately 8.9 kW to 7.7 kW, corresponding to a reduction of approximately 13.5%.

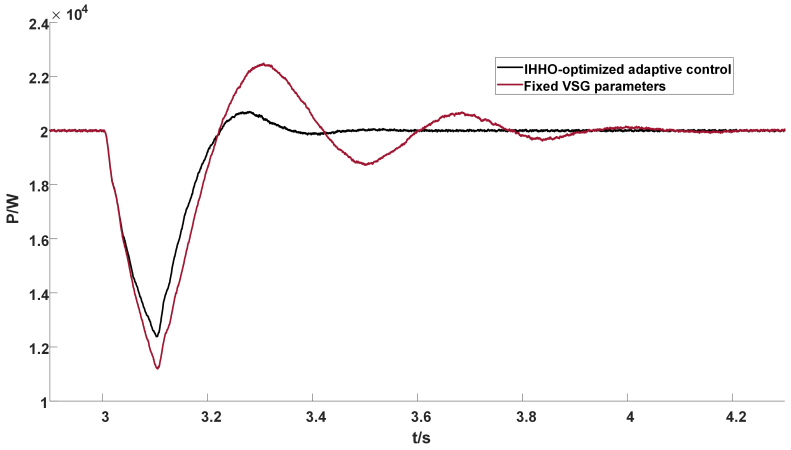


Figure 10. Active−Power Responses Under the Grid−Frequency Disturbance.

After the grid frequency returns to 50 Hz at $t = 3.1$ s, the fixed-parameter VSG exhibits a pronounced power overshoot, reaching approximately 22.5 kW, followed by several oscillations. In contrast, the IHHO-optimized adaptive VSG reaches a maximum of approximately 20.7 kW and exhibits smaller subsequent oscillations. The recovery-stage power overshoot is therefore reduced from approximately 2.5 kW to 0.7 kW, representing a reduction of approximately 72%.

Figure 11 shows the corresponding frequency-deviation responses. When the grid frequency increases at $t = 3.0$ s, both strategies exhibit an initial negative frequency deviation of approximately -0.2 Hz. Following the restoration of the nominal grid frequency at $t = 3.1$ s, the fixed-parameter VSG exhibits a positive frequency-deviation peak of approximately 0.248 Hz, whereas the IHHO-based controller limits this peak to approximately 0.154 Hz. This corresponds to a reduction of approximately 37.9%. Furthermore, the magnitude of the subsequent negative frequency-deviation peak decreases from approximately 0.073 Hz to 0.019 Hz, representing a reduction of approximately 74.0%. The smaller secondary oscillations indicate improved frequency-deviation suppression during the recovery process.

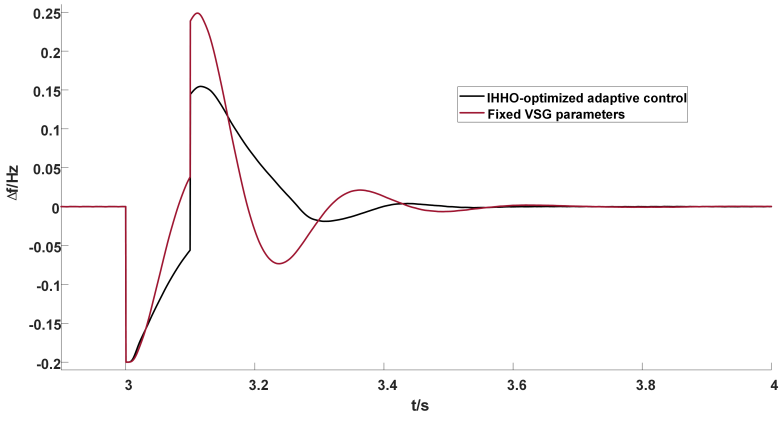


Figure 11. Frequency−Deviation Responses Under the Grid−Frequency Disturbance.

As summarized in Table 7, the estimated power settling time decreases from 0.63 s for the fixed-parameter VSG to 0.21 s for the IHHO-optimized adaptive VSG, corresponding to a reduction of approximately 66.7%. Together with the smaller power deviations and reduced frequency-deviation oscillations, these results demonstrate that the proposed IHHO-based adaptive control strategy provides improved transient recovery performance under the tested grid-frequency disturbance.

Table 7. Transient Performance Under the Grid-Frequency Disturbance.

Performance Indicator	Fixed VSG	IHHO-Based VSG
Minimum Active Power (kW)	11.1	12.3
Maximum Recovery Power (kW)	22.5	20.7
Positive Frequency-Deviation Peak (Hz)	0.248	0.154
Secondary Negative Frequency-Deviation Peak (Hz)	−0.073	−0.019
Power Settling Time (s)	0.63	0.21

Note: Power settling time is measured from $t = 3.1$ s, when the grid-frequency disturbance is removed, using a 2% error band around the 20 kW reference.

4.5. Optimization Algorithm Evaluation and Ablation Study

4.5.1. Convergence Performance and Statistical Analysis

To further investigate the optimization performance and reliability of the proposed IHHO algorithm, its convergence behavior is compared with those of GWO and HHO. The convergence curves are plotted against the cumulative number of objective-function evaluations to facilitate a fair comparison of the search progress under a common evaluation budget. In addition, multiple independent runs are conducted to assess the variability of the optimization results. The best, mean, and standard deviation of the final objective-function values are used to evaluate the solution quality and consistency of each algorithm.

Figure 12 compares the convergence behaviors of GWO, HHO, and IHHO using the cumulative number of objective-function evaluations as the horizontal axis. All evaluations, including those required by the Cauchy mutation in IHHO, are included in the evaluation count. All three algorithms exhibit rapid decreases in the best-so-far objective-function value during the initial search stage, followed by slower improvements as the search progresses. GWO shows a relatively higher final objective-function value, whereas HHO achieves a lower value. IHHO obtains the lowest final objective-function value among the three algorithms under the evaluation budget shown in the figure. These results indicate that IHHO achieves better optimization performance in terms of the final objective-function value under the tested evaluation budget.

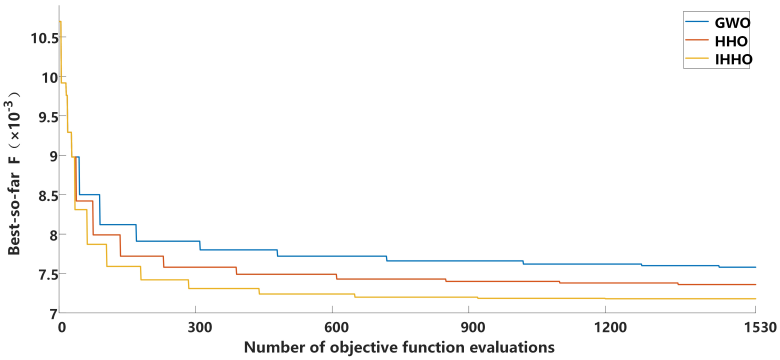


Figure 12. Convergence Curves of GWO, HHO, and IHHO Under an Equal Objective−Function Evaluation Budget.

Table 8 summarizes the optimization results obtained from ten independent runs. IHHO achieves the lowest best fitness of 7.150×10^{-3} and the lowest mean fitness of 7.187×10^{-3}, compared with 7.300×10^{-3} and 7.350×10^{-3} for HHO, and 7.540×10^{-3} and 7.584×10^{-3} for GWO, respectively. These results indicate that IHHO provides better optimization performance in terms of both the best solution and the average objective-function value. Furthermore, IHHO exhibits the smallest variance (0.000490×10^{-6}), compared with 0.000560×10^{-6} for GWO and 0.000778×10^{-6} for HHO. This indicates that

IHHO produces more consistent final objective-function values across the ten independent runs. Overall, the statistical results demonstrate that IHHO achieves a better combination of solution quality and run-to-run consistency than GWO and HHO under the tested evaluation budget.

Table 8. Statistical Comparison of Optimization Results Based on Ten Independent Runs.

Algorithm	Best Fitness ($\times 10^{-3}$)	Mean Fitness ($\times 10^{-3}$)	Variance ($\times 10^{-6}$)
GWO	7.540	7.584	0.000560
HHO	7.300	7.350	0.000778
IHHO	7.150	7.187	0.000490

4.5.2. Grid Search and Fitness Landscape Analysis

The grid search evaluates 30 values of k_j over $[0.01, 3]$ and 50 values of k_d over $[5, 50]$, resulting in 1500 candidate combinations. This evaluation budget is comparable to the maximum of 1530 objective-function evaluations used in each run of the metaheuristic algorithms.

Figure 13 illustrates the fitness distribution over the search ranges of the adaptive gains k_j and k_d. The fitness landscape exhibits a nonlinear distribution, with a relatively low-fitness region concentrated around $k_j = 1.0$–1.5 and $k_d = 28$–35. The minimum fitness obtained from the grid search is 7.1103×10^{-3}. This distribution provides a visual reference for understanding the relationship between the two adaptive gains and the objective-function value.

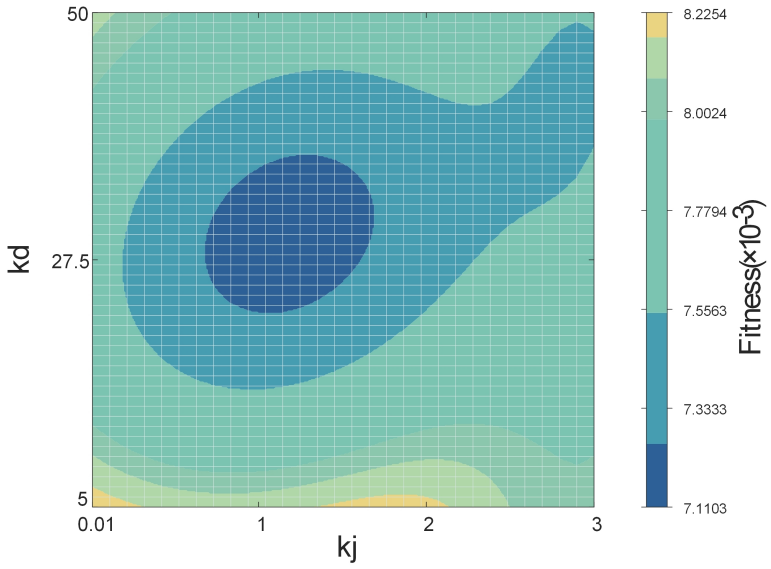


Figure 13. Two−Dimensional Fitness Landscape of the Adaptive Gains Obtained by Grid Search.

4.5.3. Computational Cost and Offline Optimization Feasibility

To compare the computational costs of GWO, HHO, and IHHO, all three algorithms are evaluated under the same maximum budget of 1530 objective-function evaluations (FEs). The evaluation count includes the initial population evaluations and all subsequent objective-function evaluations. In particular, the evaluations of candidate solutions generated by the Cauchy mutation in IHHO are included in the total evaluation budget rather than being treated as additional evaluations beyond the prescribed limit. The computational time is recorded over ten independent runs to compare the runtime performance of the three algorithms.

As shown in Table 9, the runtime of the first run is 4511.70 s for GWO, 4692.15 s for HHO, and 4702.10 s for IHHO. Across ten independent runs, the corresponding mean runtimes are 4512.31 s, 4692.30 s, and 4703.09 s, respectively. GWO exhibits the shortest mean runtime, whereas IHHO has the longest. The mean runtime of IHHO is approximately 4.23% higher than that of GWO and 0.23% higher than that of HHO.

Table 9. Computational Time and Evaluation Budget of the Compared Optimization Algorithms.

Algorithm	FEs	Run 1 (s)	Mean Runtime (s)	Standard Deviation (s)
GWO	1530	4511.70	4512.31	13.83
HHO	1530	4692.15	4692.30	15.20
IHHO	1530	4702.10	4703.09	15.20

In the proposed control framework, the IHHO algorithm is executed offline to optimize the adaptive gains k_j and k_d. Once the optimization is completed, the selected gains are incorporated into the VSG controller. During online operation, the controller adjusts the virtual inertia J and damping coefficient D_p according to the system operating state, without repeatedly executing the IHHO optimization process. Therefore, the computational time required for optimization is incurred during the offline design stage rather than within the online control loop. This arrangement avoids imposing the computational burden of the population-based optimization process on the online control loop.

Regarding real-time gain retuning, the current implementation does not execute IHHO online. The mean optimization time of approximately 4703.09 s indicates that directly repeating the complete population-based optimization process during normal VSG operation would not be suitable for fast real-time retuning under the present implementation. The current framework relies on offline gain optimization and online adaptive adjustment of virtual inertia and damping, without repeated online execution of IHHO.

4.5.4. Ablation Study of the Improved HHO Algorithm

To investigate the individual contributions of the Gold-SA exploration strategy and Cauchy mutation, an ablation study is conducted using four algorithm configurations: the original HHO, HHO with Gold-SA, HHO with Cauchy mutation, and the complete IHHO. The HHO+Gold-SA variant incorporates the Gold-SA exploration strategy without Cauchy mutation, whereas the HHO+Cauchy variant introduces Cauchy mutation without the Gold-SA strategy. The complete IHHO incorporates both modifications.

To ensure a fair comparison, all four configurations use the same objective function, search boundaries, population size, and termination criterion, with a maximum budget of 1530 objective-function evaluations per run. All objective-function evaluations associated with Cauchy mutation are included in this budget. Ten independent runs are used to evaluate the final optimization results of each configuration. The convergence curves shown in Figure 14 represent the first independent run, while the statistical results in Table 10 are calculated from all ten independent runs. The best, mean, and sample standard deviation of the final fitness values are used to assess solution quality and run-to-run variability.

As shown in Figure 14, the four configurations exhibit different convergence behaviors under the same objective-function evaluation budget. The original HHO converges to a final fitness of approximately 7.36 in the first run. After incorporating Gold-SA, the final fitness decreases to approximately 7.26, whereas the HHO+Cauchy variant reaches approximately 7.30. The complete IHHO achieves the lowest final fitness of approximately 7.18. These results indicate that both modifications can improve the optimization performance of the

original HHO in the illustrated run, with Gold-SA providing a greater improvement in the final fitness than Cauchy mutation alone.

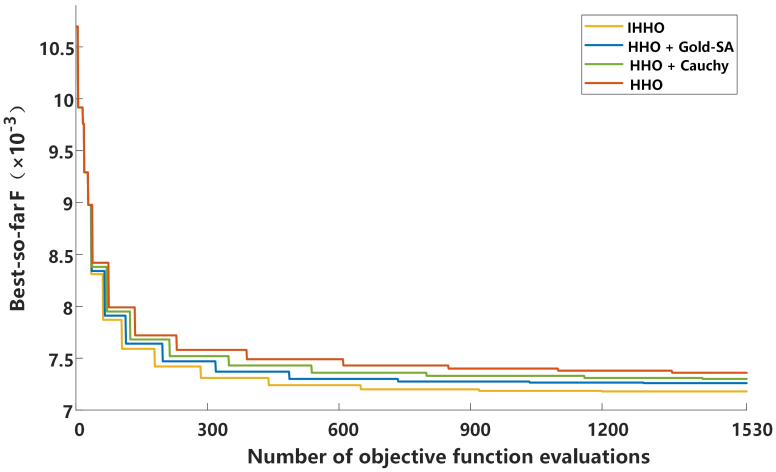


Figure 14. Convergence Curves of the Four Algorithm Configurations .

The statistical results in Table 10 further support this observation. Across ten independent runs, the mean fitness decreases from 7.350 for HHO to 7.260 for HHO+Gold-SA and 7.300 for HHO+Cauchy, corresponding to reductions of approximately 1.22% and 0.68%, respectively. The results suggest that Gold-SA contributes more strongly to improving the average solution quality under the tested conditions, while Cauchy mutation also provides a measurable improvement over the original HHO.

Table 10. Statistical Results of the Ablation Study.

Algorithm	Best Fitness ($\times 10^{-3}$)	Mean Fitness ($\times 10^{-3}$)	Standard Deviation ($\times 10^{-3}$)
HHO	7.300	7.350	0.0279
HHO + Gold-SA	7.180	7.260	0.0368
HHO + Cauchy	7.270	7.300	0.0200
IHHO	7.150	7.187	0.0221

The complete IHHO achieves a best fitness of 7.150 and a mean fitness of 7.187, corresponding to an approximately 2.22% reduction in mean fitness relative to the original HHO. Its mean fitness is also lower than those of HHO+Gold-SA and HHO+Cauchy by approximately 1.01% and 1.55%, respectively. This indicates that combining the two modifications produces the best overall solution quality among the four configurations in these experiments.

Regarding run-to-run variability, HHO+Cauchy has the smallest standard deviation of 0.0200, followed by IHHO at 0.0221, HHO at 0.0279, and HHO+Gold-SA at 0.0368. Thus, although Gold-SA achieves a lower mean fitness when used individually, its results exhibit greater variability across the ten runs. The complete IHHO combines a lower mean fitness with a smaller standard deviation than the original HHO and the HHO+Gold-SA variant, although it does not achieve the smallest standard deviation among all configurations.

Overall, the ablation results demonstrate that Gold-SA and Cauchy mutation make distinct contributions to the optimization process. Gold-SA provides a greater improvement in mean solution quality when used individually, whereas Cauchy mutation yields lower run-to-run variability in the tested experiments. The complete IHHO achieves the best mean and best individual fitness among the four configurations, supporting the effectiveness of incorporating both modifications in the proposed algorithm.

4.6. Sensitivity Analysis

4.6.1. Sensitivity Analysis of Adaptive-Law Scaling Parameters

To investigate the influence of the scaling coefficients on the dynamic performance of the adaptive VSG, a sensitivity analysis is conducted for the parameters α and β. Based on the adaptive control laws introduced in Section 2, the virtual inertia and damping coefficient can be expressed in terms of these scaling coefficients as follows:

$$J^*(x_1, x_2) = J_0 + \frac{2k_j}{\pi} \arctan(\alpha|x_1|) \left[\frac{1 + \tanh(\beta x_1 x_2)}{2} + 0.1 \frac{1 - \tanh(\beta x_1 x_2)}{2} \right]. \quad (25)$$

$$D_p^*(x_1) = D_{p0} + \frac{3}{2} \pi k_d \tanh(\beta|x_1|). \quad (26)$$

In the adaptive control laws, α determines the sensitivity of the arctangent-based virtual inertia adjustment, while β influences both the inertia weighting function and the adaptive damping response. To investigate their effects on transient performance, a one-factor-at-a-time sensitivity analysis is conducted. The IHHO-optimized adaptive gains are kept unchanged throughout the experiments, and no additional optimization is performed. Specifically, α is varied over $\{6, 8, 10, 12, 14\}$ while β is fixed at 0.1. Similarly, β is varied over $\{0.06, 0.08, 0.10, 0.12, 0.14\}$ while α is fixed at 10. The same two active-power reference steps used in the preceding comparative experiments are adopted: 0 to 10 kW at $t = 0.2$ s and 10 to 20 kW at $t = 1.0$ s. The overshoot and settling time are employed to evaluate the sensitivity of the transient responses.

Figures 15 and 16 illustrate the influence of α on the transient response when $\beta = 0.1$. As α varies from 6 to 14, the overshoot ranges from 5.3% to 6.8% for the first power step and from 6.8% to 8.1% for the second step. Meanwhile, the settling time of the first step remains within a narrow range of 0.26–0.28 s, indicating relatively limited variation in the corresponding recovery time. For the second power step, the selected value $\alpha = 10$ achieves the shortest settling time of 0.24 s among the investigated values. At this setting, the corresponding overshoots are 5.7% and 7.2% for the first and second steps, respectively. These results suggest that $\alpha = 10$ provides a favorable balance between overshoot suppression and transient recovery speed.

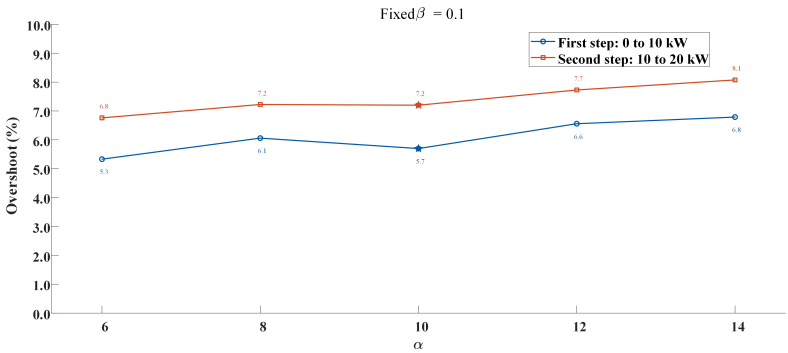


Figure 15. Sensitivity of Active−Power Overshoot to the Scaling Coefficient α .

Figures 17 and 18 present the sensitivity results for β with $\alpha = 10$. Increasing β from 0.06 to 0.14 reduces the overshoot of the first step from 10.0% to 4.8% and that of the second step from 11.5% to 5.8%. These results demonstrate that β plays an important role in regulating transient power overshoot through the nonlinear inertia weighting and adaptive damping mechanisms.

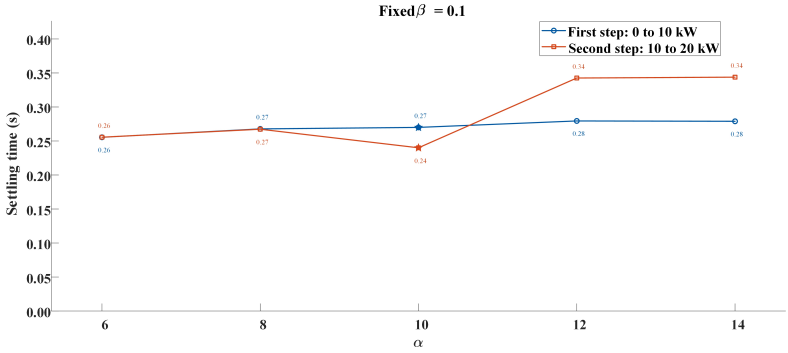


Figure 16. Sensitivity of Settling Time to the Scaling Coefficient α .

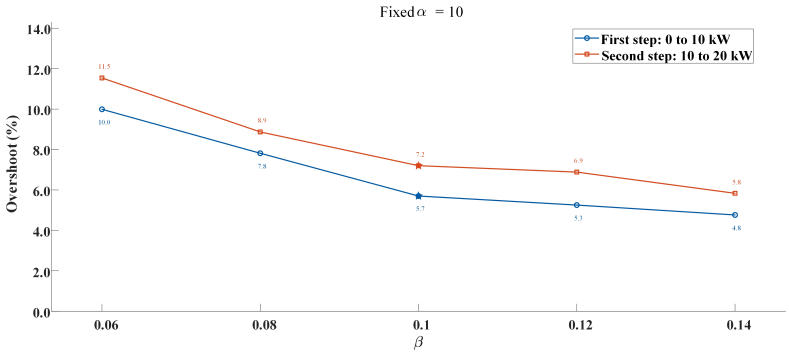


Figure 17. Sensitivity of Active−Power Overshoot to the Scaling Coefficient β .

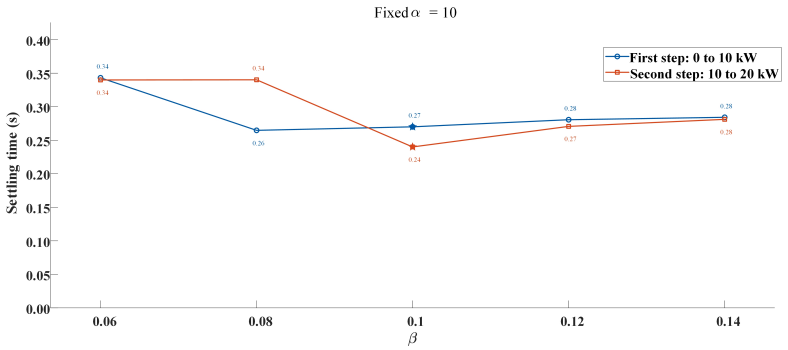


Figure 18. Sensitivity of Settling Time to the Scaling Coefficient β .

The settling-time responses further indicate that the selected value $\beta = 0.1$ achieves the shortest second-step settling time of 0.24 s among the tested values, while maintaining a first-step settling time of 0.27 s. Although larger values of β provide further overshoot suppression, the selected coefficient maintains a favorable combination of moderate overshoot and rapid transient recovery.

Overall, the sensitivity analysis confirms that the two scaling coefficients have different influences on the dynamic performance of the adaptive VSG controller. The coefficient α mainly affects the inertia adjustment characteristics, whereas β influences both the inertia weighting and damping adjustment. Within the investigated parameter ranges, the selected values $\alpha = 10$ and $\beta = 0.1$ provide a favorable compromise between transient overshoot and settling time. The results therefore provide simulation-based justification for the adopted scaling coefficients under the investigated operating conditions. Furthermore, the additional power-step tests presented in Section 4.4.1 demonstrate that the adopted scaling coefficients also provide satisfactory transient performance under different power-reference magnitudes and directions, without further parameter adjustment. Together with the sensitivity results presented in this subsection, these findings support the practical selection of $\alpha = 10$ and $\beta = 0.1$ for the investigated operating conditions.

4.6.2. Sensitivity Analysis of Gain-Search Boundaries

The baseline search ranges were selected as practical optimization bounds based on the roles of the adaptive gains in the nonlinear control laws. The gain k_j determines the magnitude of virtual-inertia adaptation, whereas k_d governs the strength of damping adaptation. The lower and upper limits were chosen to cover a broad range of adaptation strengths while avoiding unnecessarily extreme candidate gains. These intervals are practical search bounds rather than uniquely determined theoretical limits. Their suitability is therefore further assessed by comparing the baseline ranges with narrower and expanded search domains under the same optimization budget.

To investigate the sensitivity of the optimized adaptive gains to the prescribed search boundaries, three search-boundary settings were considered. Setting A corresponds to the original search ranges, $k_j \in [0.01, 3]$ and $k_d \in [5, 50]$. Setting B adopts narrower ranges, $k_j \in [0.5, 2]$ and $k_d \in [15, 40]$, whereas Setting C uses expanded ranges, $k_j \in [0.005, 4]$ and $k_d \in [2.5, 60]$. For each setting, ten independent optimization runs were conducted using independently generated initial populations. The population size was fixed at 30, and the maximum iteration count was set to 50, subject to a hard limit of 1530 objective-function evaluations per run. All objective-function evaluations, including those associated with Cauchy mutation, were counted toward this budget. The fitness function and all other optimization settings were kept identical across the three settings. The final best fitness values and corresponding optimized gains were recorded for each run.

Figure 19 compares the optimized gain distributions obtained under the three search-boundary settings. Under Settings A and B, the optimized gains are concentrated in similar regions. The observed k_j values range from 0.91 to 1.00 under Setting A and from 0.91 to 1.01 under Setting B. The corresponding k_d values range from 29.6 to 30.8 and from 29.4 to 30.8, respectively. The substantial overlap between these distributions indicates that narrowing the prescribed search boundaries within the tested intervals has little effect on the region in which high-quality gain combinations are identified.

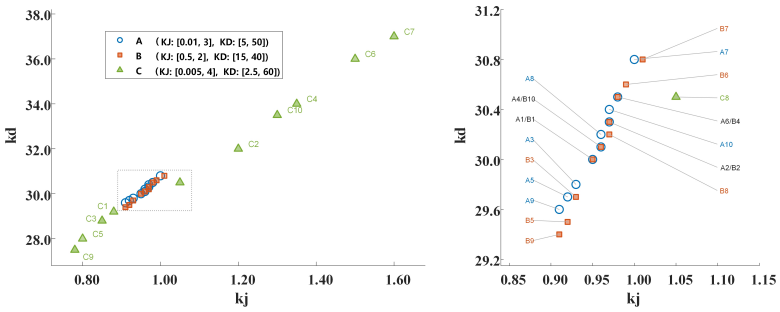


Figure 19. Distribution of the optimized adaptive gains under three search−boundary settings. The right panel provides a magnified view of the clustered region in the left panel.

In contrast, Setting C produces a wider distribution of optimized gains, with k_j ranging from 0.78 to 1.60 and k_d ranging from 27.5 to 37.0. Nevertheless, all ten optimized gain pairs obtained under Setting C remain within the narrower search intervals of Setting B. In particular, the gain pair associated with the lowest fitness value under Setting C is $k_j = 0.78$ and $k_d = 27.5$, which also satisfies the bounds of Setting B. Therefore, the expanded search domain allows a wider distribution of optimized solutions, but the observed results do not demonstrate that the expanded boundaries are necessary to identify this low-fitness solution.

The final fitness values in Figure 20 provide a complementary comparison of optimization performance across independent runs. Under Setting A, the fitness values range from 7.15 to 7.22, whereas those under Setting B range from 7.16 to 7.21. The two settings

therefore produce similar fitness levels across the ten runs. Setting C exhibits a wider range, from 7.08 to 7.30. Although Setting C achieves the lowest individual fitness value among the three settings, it also produces the highest individual value. This contrast indicates that the lower best fitness obtained under the expanded search boundaries is accompanied by greater variability between independent runs.

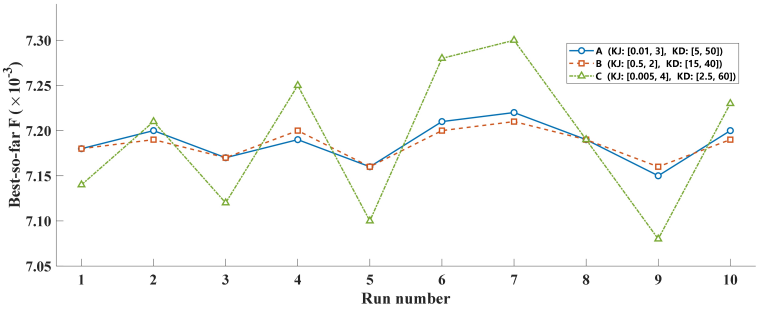


Figure 20. Final best fitness values obtained in ten independent optimization runs under the three search−boundary settings. The connecting lines are used only to facilitate visual comparison across run indices.

The results also provide evidence regarding the repeatability of IHHO under different random initial populations. For the original search boundaries, the mean final fitness is 7.187, with a sample standard deviation of 0.0221. The relatively concentrated distribution across ten independent runs indicates that IHHO produces comparable optimization results under repeated random initialization with the original search configuration. However, the observed run-to-run variability reflects the combined effects of random initialization and stochastic optimization operations. Because the initial population quality was not independently controlled, these results assess repeatability across random initializations rather than isolating the individual causal effect of initial population quality.

The quantitative results are summarized in Table 11. The mean fitness values under Settings A, B, and C are 7.187, 7.185, and 7.190, respectively. The difference between the highest and lowest mean values is only 0.005. Their corresponding sample standard deviations are 0.0221, 0.0172, and 0.0770. In particular, the standard deviation under Setting C is approximately 3.48 times that under Setting A and 4.48 times that under Setting B. Thus, expanding the search boundaries does not improve the mean fitness in these experiments, despite producing a lower individual best value. Settings A and B exhibit comparable mean performance, while Setting B has the smallest observed standard deviation.

Table 11. Sensitivity of optimization results to gain-search boundaries.

Setting	k_j Search Range	k_d Search Range	Best Fitness ($\times 10^{-3}$)	Mean Fitness ($\times 10^{-3}$)	Sample SD ($\times 10^{-3}$)	Observed k_j^* Range	Observed k_d^* Range
A (Original)	$[0.01, 3]$	$[5, 50]$	7.15	7.187	0.0221	$[0.91, 1.00]$	$[29.6, 30.8]$
B (Narrower)	$[0.5, 2]$	$[15, 40]$	7.16	7.185	0.0172	$[0.91, 1.01]$	$[29.4, 30.8]$
C (Expanded)	$[0.005, 4]$	$[2.5, 60]$	7.08	7.190	0.0770	$[0.78, 1.60]$	$[27.5, 37.0]$

Note: Each setting was evaluated in ten independent optimization runs using independently generated initial populations. SD denotes the sample standard deviation of the final best fitness values. Lower fitness values indicate better optimization performance. The observed optimized-gain ranges represent the minimum and maximum values across the ten runs, rather than the prescribed search boundaries. Fitness values are reported on the numerical scale used in the fitness data.

Overall, the results support the practical suitability of the original gain-search boundaries for the investigated VSG model and fitness function. The close agreement between Settings A and B in terms of mean fitness and optimized-gain distributions suggests that

the identified high-quality solutions are relatively stable against the tested reduction in search ranges. Although Setting C yields a lower best fitness in one run, its mean fitness does not improve and its run-to-run variability is substantially greater.

4.6.3. Sensitivity Analysis of Combined IHHO Parameter Settings

To further investigate the influence of algorithm settings on the optimization performance of IHHO, a sensitivity analysis was conducted by jointly varying the population size N and the Cauchy mutation probability P_c. Three parameter combinations were considered: $(N, P_c) = (30, 0.2)$, $(20, 0.1)$, and $(40, 0.3)$, denoted as Settings A, B, and C, respectively. Setting A corresponds to the original configuration adopted in this study. For each setting, ten independent optimization runs were performed using different random initial populations. The gain-search boundaries, fitness function, and other algorithm parameters were kept unchanged. The same objective-function evaluation budget was applied to the three settings to ensure a consistent comparison.

Figure 21 illustrates the distribution of the optimized adaptive gains obtained under the three parameter settings. Under the baseline Setting A, the optimized gains are concentrated within relatively narrow ranges, with k_j varying from 0.91 to 1.00 and k_d varying from 29.6 to 30.8. The magnified view further demonstrates the consistency of the optimized gain combinations across the ten independent runs.

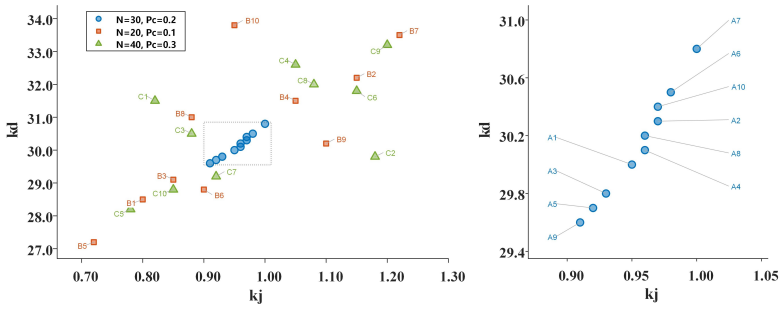


Figure 21. Distribution of the optimized adaptive gains under three IHHO parameter settings. The right panel provides a magnified view of the optimized gains obtained under the baseline Setting A.

In comparison, Settings B and C exhibit wider distributions of optimized gains. For Setting B, the observed ranges of k_j and k_d are 0.72–1.22 and 27.2–33.8, respectively. For Setting C, the corresponding ranges are 0.78–1.20 and 28.2–33.2. These results indicate that the original parameter combination produces more concentrated optimized gains than the two alternative combinations under the investigated conditions.

Figure 22 compares the final best fitness values obtained from ten independent runs under the three parameter settings. Setting A consistently achieves lower fitness values than Settings B and C. Specifically, the fitness values under Setting A range from 7.15×10^{-3} to 7.22×10^{-3}, whereas those under Settings B and C range from 7.26×10^{-3} to 7.40×10^{-3} and from 7.24×10^{-3} to 7.35×10^{-3}, respectively. Notably, even the highest fitness value under Setting A is lower than the lowest values obtained under the two alternative settings. This observation demonstrates the favorable optimization performance of the original parameter combination across the investigated runs.

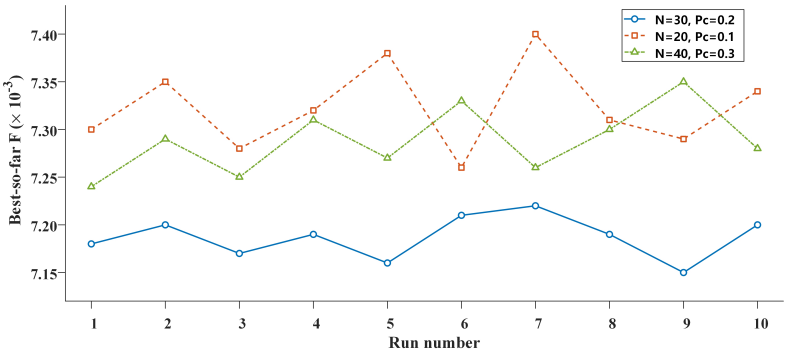


Figure 22. Final best fitness values obtained in ten independent optimization runs under three IHHO parameter settings.

The statistical results are summarized in Table 12. The mean fitness values for Settings A, B, and C are 7.187×10^{-3}, 7.323×10^{-3}, and 7.288×10^{-3}, respectively. Compared with Setting A, the mean fitness increases by approximately 1.89% and 1.41% under Settings B and C. Furthermore, Setting A achieves the smallest sample standard deviation of 0.0221×10^{-3}, compared with 0.0445×10^{-3} and 0.0352×10^{-3} for Settings B and C. These findings indicate that the original parameter combination achieves both favorable fitness performance and relatively low run-to-run variability.

Table 12. Sensitivity of IHHO optimization results to combined algorithm parameter settings. .

Setting	N	P_c	Best Fitness ($\times 10^{-3}$)	Mean Fitness ($\times 10^{-3}$)	Sample SD ($\times 10^{-3}$)	Observed Gain Ranges
A (Baseline)	30	0.2	7.15	7.187	0.0221	k_j^* : [0.91, 1.00]; k_d^* : [29.6, 30.8]
B (Reduced)	20	0.1	7.26	7.323	0.0445	k_j^* : [0.72, 1.22]; k_d^* : [27.2, 33.8]
C (Increased)	40	0.3	7.24	7.288	0.0352	k_j^* : [0.78, 1.20]; k_d^* : [28.2, 33.2]

Note: Each setting was evaluated over ten independent optimization runs. SD denotes the sample standard deviation of the final best fitness values. Lower fitness values indicate better optimization performance. The observed gain ranges indicate the minimum and maximum optimized gains across the ten runs.

Overall, the sensitivity analysis demonstrates that the baseline setting of $N = 30$ and $P_c = 0.2$ provides a favorable combination of optimization accuracy and repeatability under the investigated conditions. Compared with the two alternative settings, the baseline configuration achieves the lowest mean fitness, the smallest sample standard deviation, and more concentrated optimized adaptive gains. These results provide experimental support for the adopted IHHO parameter configuration. Since the population size and mutation probability were varied simultaneously, the findings describe the combined influence of these parameters rather than their individual contributions.

5. Conclusions

This paper proposes an improved Harris Hawks optimization (IHHO)-based adaptive VSG control strategy to improve transient response and overshoot suppression. Bounded nonlinear control laws are developed for virtual inertia J and damping coefficient D_p, and a dimensionless multi-index objective function is used to jointly optimize the adaptation gains k_j and k_d.

Under consecutive active-power steps from 0 to 10 kW and from 10 to 20 kW, the proposed method achieves overshoots of 5.7% and 7.2% and settling times of 0.27 s and 0.24 s, respectively. The frequency-response analysis also shows reductions of approximately 50% in negative frequency-deviation peaks and 41% in negative ROCOF peaks under the

investigated conditions. The ablation study confirms the complementary contributions of Gold-SA and Cauchy mutation, with the complete IHHO achieving a mean fitness of 7.187×10^{-3}. Sensitivity analyses show that expanding the gain-search boundaries does not improve mean fitness and increases run-to-run variability, while the baseline algorithm setting of $N = 30$ and $P_c = 0.2$ performs best among the tested parameter combinations.

Additional tests involving three consecutive power-reference steps and a grid-frequency disturbance from 50 to 50.2 Hz followed by a return to 50 Hz further evaluate the controller under different operating conditions. IHHO is executed offline, with a maximum budget of 1530 objective-function evaluations per run and a mean optimization time of 4703.09 s. The resulting gains are then used by the online adaptive VSG controller without repeated execution of IHHO.

Future work will investigate measurement noise, grid-impedance variations, voltage dips, load-step disturbances, weaker-grid conditions, and broader power and frequency disturbances. Computational acceleration for gain retuning and hardware-in-the-loop validation will also be explored.

Author Contributions: Conceptualization, R.H. and Z.C.; methodology, R.H., T.Y. and Z.C.; investigation, R.H., T.Y., T.P. and D.X.; resources, R.H. and T.P.; original draft preparation, R.H. and T.Y.; review and editing, R.H., T.Y., T.P., C.Z., Z.C. and D.X.; supervision, T.P., T.Y. and C.Z.; project administration, C.Z. and T.Y.; funding acquisition, D.X. All authors have read and agreed to the published version of the manuscript.

Funding: This work is supported by the National Natural Science Foundation of China (No. 62573211).

Data Availability Statement: The data presented in this study are available upon request from the corresponding author. For privacy reasons, these data are not publicly available.

Conflicts of Interest: The authors declares no conflicts of interest.

References

1. Bevrani, H.; Ise, T.; Miura, Y. Virtual Synchronous Generators: A Survey and New Perspectives. *Int. J. Electr. Power Energy Syst.* **2014**, *54*, 244–254. https://doi.org/10.1016/j.ijepes.2013.07.009.
2. Cheema, K.M. A Comprehensive Review of Virtual Synchronous Generator. *Int. J. Electr. Power Energy Syst.* **2020**, *120*, 106006. https://doi.org/10.1016/j.ijepes.2020.106006.
3. Zhang, H.; Xiang, W.; Lin, W.; Wen, J. Grid Forming Converters in Renewable Energy Sources Dominated Power Grid: Control Strategy, Stability, Application, and Challenges. *J. Mod. Power Syst. Clean Energy* **2021**, *9*, 1239–1256. https://doi.org/10.35833/MPCE.2021.000257.
4. Xu, H.; Yu, C.; Liu, C.; Wang, Q.; Zhang, X. An Improved Virtual Inertia Algorithm of Virtual Synchronous Generator. *J. Mod. Power Syst. Clean Energy* **2020**, *8*, 377–386. https://doi.org/10.35833/MPCE.2018.000472.
5. Zhong, Q.C.; Nguyen, P.L.; Ma, Z.; Sheng, W. Self-Synchronized Synchronverters: Inverters Without a Dedicated Synchronization Unit. *IEEE Trans. Power Electron.* **2014**, *29*, 617–630. https://doi.org/10.1109/TPEL.2013.2258684.
6. Fang, J.; Li, H.; Tang, Y.; Blaabjerg, F. Distributed Power System Virtual Inertia Implemented by Grid-Connected Power Converters. *IEEE Trans. Power Electron.* **2018**, *33*, 8488–8499. https://doi.org/10.1109/TPEL.2017.2785218.
7. Tayyebi, A.; Groß, D.; Anta, A.; Kupzog, F.; Dörfler, F. Frequency Stability of Synchronous Machines and Grid-Forming Power Converters. *IEEE J. Emerg. Sel. Top. Power Electron.* **2020**, *8*, 1004–1018. https://doi.org/10.1109/JESTPE.2020.2966524.
8. Li, S.; Gu, S. A Theoretical Study on Coordinated Control Strategy of VSG for Transient Power Angle Stability and Fault Current Limiting. *Appl. Syst. Innov.* **2026**, *9*, 109. https://doi.org/10.3390/asi9060109.
9. Meng, X.; Liu, J.; Liu, Z. A Generalized Droop Control for Grid-Supporting Inverter Based on Comparison Between Traditional Droop Control and Virtual Synchronous Generator Control. *IEEE Trans. Power Electron.* **2019**, *34*, 5416–5438. https://doi.org/10.1109/TPEL.2018.2868722.
10. Mottaghizadeh, M.; Soltani, S.; Kamwa, I.; Rabiee, A.; Mohseni-Bonab, S.M. Impact of Wind Speed Variations on Frequency Control in Grid-Forming PMSG-Based Wind Turbines. *Appl. Syst. Innov.* **2026**, *9*, 94. https://doi.org/10.3390/asi9050094.

11. Niu, G.; Ji, Y.; Wu, M.; Zheng, N.; Liu, Y.; Yan, X.; Gan, Y. Autonomous Frequency–Voltage Regulation Strategy for Weak-Grid Renewable-Energy Stations Based on Hybrid Supercapacitors and Cascaded H-Bridge Converters. *Appl. Syst. Innov.* **2026**, *9*, 23. https://doi.org/10.3390/asi9010023.
12. Ur Rehman, H.; Yan, X.; Abdelbaky, M.A.; Jan, M.U.; Iqbal, S. An Advanced Virtual Synchronous Generator Control Technique for Frequency Regulation of Grid-Connected PV System. *Int. J. Electr. Power Energy Syst.* **2021**, *125*, 106440. https://doi.org/10.1016/j.ijepes.2020.106440.
13. Shaharear, M.A.; Zhou, C.; Shaikh, S.; Faruk, M.M.H. Load Frequency Control in Multi-Area Power Systems Using Incremental Proportional–Integral–Derivative and Model-Free Adaptive Control. *Appl. Syst. Innov.* **2026**, *9*, 59. https://doi.org/10.3390/asi9030059.
14. Cheng, H.; Shuai, Z.; Shen, C.; Liu, X.; Li, Z.; Shen, Z.J. Transient Angle Stability of Paralleled Synchronous and Virtual Synchronous Generators in Islanded Microgrids. *IEEE Trans. Power Electron.* **2020**, *35*, 8751–8765. https://doi.org/10.1109/TPEL.2020.2965152.
15. Othman, M.H.; Mokhlis, H.; Mubin, M.; Talpur, S.; Ab Aziz, N.F.; Dradi, M.; Mohamad, H. Progress in Control and Coordination of Energy Storage System-Based VSG: A Review. *IET Renew. Power Gener.* **2020**, *14*, 177–187. https://doi.org/10.1049/iet-rpg.2019.0274.
16. Skiparev, V.; Machlev, R.; Chowdhury, N.R.; Levron, Y.; Petlenkov, E.; Belikov, J. Virtual Inertia Control Methods in Islanded Microgrids. *Energies* **2021**, *14*, 1562. https://doi.org/10.3390/en14061562.
17. Xiao, J.; Jia, Y.; Jia, B.; Li, Z.; Pan, Y.; Wang, Y. An Inertial Droop Control Based on Comparisons Between Virtual Synchronous Generator and Droop Control in Inverter-Based Distributed Generators. *Energy Rep.* **2020**, *6*, 104–112. https://doi.org/10.1016/j.egyr.2020.12.003.
18. D'Arco, S.; Suul, J.A.; Fosso, O.B. A Virtual Synchronous Machine Implementation for Distributed Control of Power Converters in SmartGrids. *Electr. Power Syst. Res.* **2015**, *122*, 180–197. https://doi.org/10.1016/j.epsr.2015.01.001.
19. Heidari, A.A.; Mirjalili, S.; Faris, H.; Aljarah, I.; Mafarja, M.; Chen, H. Harris Hawks Optimization: Algorithm and Applications. *Future Gener. Comput. Syst.* **2019**, *97*, 849–872. https://doi.org/10.1016/j.future.2019.02.028.
20. Mirjalili, S. SCA: A Sine Cosine Algorithm for Solving Optimization Problems. *Knowl.-Based Syst.* **2016**, *96*, 120–133. https://doi.org/10.1016/j.knosys.2015.12.022.
21. Tanyildizi, E.; Demir, G. Golden Sine Algorithm: A Novel Math-Inspired Algorithm. *Adv. Electr. Comput. Eng.* **2017**, *17*, 71–78. https://doi.org/10.4316/AECE.2017.02010.
22. Tanyildizi, E. A Novel Optimization Method for Solving Constrained and Unconstrained Problems: Modified Golden Sine Algorithm. *Turk. J. Electr. Eng. Comput. Sci.* **2018**, *26*, 3287–3304. https://doi.org/10.3906/elk-1802-232.
23. Wu, L.; Wu, J.; Wang, T. The Improved Grasshopper Optimization Algorithm with Cauchy Mutation Strategy and Random Weight Operator for Solving Optimization Problems. *Evol. Intell.* **2024**, *17*, 1751–1781. https://doi.org/10.1007/s12065-023-00861-z.
24. Wang, M.; Wang, J.S.; Li, X.D.; Zhang, M.; Hao, W.K. Harris Hawk Optimization Algorithm Based on Cauchy Distribution Inverse Cumulative Function and Tangent Flight Operator. *Appl. Intell.* **2022**, *52*, 10999–11026. https://doi.org/10.1007/s10489-021-03080-0.
25. Yao, X.; Liu, Y.; Lin, G. Evolutionary Programming Made Faster. *IEEE Trans. Evol. Comput.* **1999**, *3*, 82–102. https://doi.org/10.1109/4235.771163.
26. Wolpert, D.H.; Macready, W.G. No Free Lunch Theorems for Optimization. *IEEE Trans. Evol. Comput.* **1997**, *1*, 67–82. https://doi.org/10.1109/4235.585893.
27. Zhang, X.; Li, D.; Yang, Z.; Tian, L.; Meng, J.; Liu, Y.; Fu, C. Fuzzy Adaptive Virtual Inertia Control of Energy Storage Systems Considering SOC Constraints. *Energy Rep.* **2023**, *9*, 2431–2439. https://doi.org/10.1016/j.egyr.2023.01.078.
28. Lyu, L.; Wang, X.; Zhang, L.; Zhang, Z.; Koh, L.H. Fuzzy Control Based Virtual Synchronous Generator for Self-Adaptative Control in Hybrid Microgrid. *Energy Rep.* **2022**, *8*, 12092–12104. https://doi.org/10.1016/j.egyr.2022.09.055.
29. Fang, H.; Yu, Z. Control of Virtual Synchronous Generator for Frequency Regulation Using a Coordinated Self-Adaptive Method. *CSEE J. Power Energy Syst.* **2024**, *10*, 175–184. https://doi.org/10.17775/CSEEJPES.2020.01950.
30. Li, L.; Sun, Y.; Liu, Y.; Tian, P.; Shen, S. A Communication-Free Adaptive Virtual Inertia Control of Cascaded-Type VSGs for Power Oscillation Suppression. *Int. J. Electr. Power Energy Syst.* **2023**, *149*, 109034. https://doi.org/10.1016/j.ijepes.2023.109034.
31. Ling, Z.; Liu, Y.; Wang, Z.; Yin, J. Adaptive Inertia and Damping of Grid-Connected Inverter with Improved VSG Control. *IET Power Electron.* **2023**, *16*, 2769–2781. https://doi.org/10.1049/pel2.12600.
32. Shi, T.; Sun, J.; Han, X.; Tang, C. Research on Adaptive Optimal Control Strategy of Virtual Synchronous Generator Inertia and Damping Parameters. *IET Power Electron.* **2024**, *17*, 121–133. https://doi.org/10.1049/pel2.12620.
33. Storn, R.; Price, K. Differential Evolution—A Simple and Efficient Heuristic for Global Optimization Over Continuous Spaces. *J. Glob. Optim.* **1997**, *11*, 341–359. https://doi.org/10.1023/A:1008202821328.
34. Awda, Y.; Alowaifeer, M. Adaptive Optimization of Virtual Synchronous Generator Based on Fuzzy Logic Control and Differential Evolution. *Ain Shams Eng. J.* **2024**, *15*, 102606. https://doi.org/10.1016/j.asej.2023.102606.

35. Xiong, K.; Hu, W.; Zhang, G.; Zhang, Z.; Chen, Z. Deep Reinforcement Learning Based Parameter Self-Tuning Control Strategy for VSG. *Energy Rep.* **2022**, *8*, 219–226. https://doi.org/10.1016/j.egyr.2022.02.147.
36. Mirjalili, S.; Mirjalili, S.M.; Lewis, A. Grey Wolf Optimizer. *Adv. Eng. Softw.* **2014**, *69*, 46–61. https://doi.org/10.1016/j.advengsoft.2013.12.007.

Disclaimer/Publisher's Note: The statements, opinions and data contained in all publications are solely those of the individual author(s) and contributor(s) and not of MDPI and/or the editor(s). MDPI and/or the editor(s) disclaim responsibility for any injury to people or property resulting from any ideas, methods, instructions or products referred to in the content.